Shock Waves (2003) 13: 299–322
Digital Object Identifier (DOI) 10.1007/s00193-003-0217-y

Shock Waves

Numerical investigations of shock waves in gas-particle mixtures

Evaluation of numerical methods for dusty-gas shock wave phenomena

T. Saito, M. Marumoto, K. Takayama

Interdisciplinary Shock Wave Research Laboratory, Institute of Fluid Science, Tohoku University, 2-1-1 Katahira, Aoba-ku, Sendai 980-8577, Japan

Received 22 May 2003 / Accepted 28 August 2003
Published online 12 November 2003 – © Springer-Verlag 2003
Communicated by H. Grönig

Abstract. The propagation of shock waves in gas-particle mixtures in one- and two-dimensional geometries is numerically investigated. Two schemes for approximating conservation laws for particles, which are collectively treated as a continuum medium, are compared and discussed. Different models of the drag coefficient and Nusselt number, directly affecting the interaction between the gas and particle phases, are used for obtaining shock profiles, and the results are compared. The oblique shock reflections at a solid wedge in a gas-particle mixture are simulated. The results demonstrate that the reflection pattern changes as the shock propagates along the wedge, revealing strong non-selfsimilarity of the phenomenon.

Key words: Dusty gas, Shock wave, CFD, Drag coefficient, Nusselt number, Oblique shock reflection

1 Introduction

Over many decades, numerous scientists have investigated the dynamics of two phase flows of gaseous media loaded with small solid particles (dusty gases). The research field is directly linked to some important applications, such as shock wave interactions with solid particles in a solid-fuel-booster nozzle, high speed flights in the rain, snow, dust etc. The studies of the mechanism of accidental explosions in coal mines or grain silos are also important for establishing better safety measures. As a result, there are many publications devoted to different aspects of the phenomena as well as review articles (Nettleton 1977; Igra and Ben-Dor 1988).

High-speed flows of dusty gases, especially non-stationary ones, are quite different from their pure gas counterparts due to momentum and energy exchange between the two phases. The solid particles cannot follow rapid changes in the gas velocity and temperature, exhibiting non-equilibrium shock regions behind shock wave fronts. The thickness and structure of the non-equilibrium shock regions were investigated by Carrier (1958), Kriebel (1964) and Rudinger (1964). Rudinger (1965) also investigated the effect of particle volume on the flow. The non-stationary phenomena of shock wave interactions in dusty gases were studied numerically by Otterman and Levine (1974) and Miura and Glass (1982). As more and more computational power became readily available, numerical simulations of multi-dimensional complex dusty-gas flows, such as two-dimensional nozzle flows and the flows with boundary layers, were performed (Saurel et al. 1994; Sainsaulieu 1995; Igra et al. 1999; Thevand et al. 1999; Slater and Young 2001).

The study of shock reflections at a solid wall is one of the important and fundamental research subjects. Kim and Chang (1991) numerically simulated the oblique shock reflections and investigated the effects of particle size and loading ratio on the reflection pattern of single Mach reflection (SMR). Ben-Dor et al. (2001) also studied oblique shock reflections in dusty gases, considering not only SMR but also transitional Mach reflection (TMR), double Mach reflection (DMR) and regular reflection (RR).

Despite the extensive research efforts in the past, quite a lot of dusty-gas problems are still unsolved. In the numerical simulations of shock wave interactions or propagation in dusty gases, many assumptions are usually made. Some of them are reasonable, while others are accepted solely for the convenience of numerical analysis. In order to reduce the number of such assumptions in the dusty-gas flow simulations, it is necessary to propose a good mathematical model for each physical process and substantiate it with reliable experimental data.

In this study, we first compare two different numerical schemes for solving the particle phase. The effects of different mathematical models for the drag coefficient and Nusselt number are then investigated. The numerical analysis of oblique shock reflections is carried out at the next stage, demonstrating their non-selfsimilarity. The

Correspondence to: T. Saito,
(e-mail: saito@bellanca.ifs.tohoku.ac.jp)

information gained from the series of numerical analysis provides a valuable precept for designing dusty shock wave experiments which is now being prepared in our laboratory.

2 One-dimensional dusty-gas flows

Numerical analysis of one-dimensional dusty-gas flows is described in this section. The interaction between the gas and solid particle phases is effected by the drag force and heat exchange. These are included as source terms into the basic conservation equations for the two phases. Therefore, it is possible to employ different numerical schemes for each phase as long as they can handle the source terms properly. In this study, the weighted average flux (WAF) finite-volume method of Toro (1989) is used for the gas phase. As to the solid particle phase, two different schemes are implemented. The numerical results are compared and discussed for a simple shock tube problem. Many different mathematical models for the drag coefficient and Nusselt number have been proposed in the past, and the evaluation of those models is also done in this section.

2.1 Basic equations

The following assumptions are universally adopted in the studies of dusty-gas flows. We follow them as well:

- the gas obeys the perfect equation of state;
- the number density of particles is large enough so that the particles could be considered as a continuum;
- the particles' volume is negligible;
- particles do not collide with each other so that they do not contribute to pressure;
- particles are spherical and of the same diameter; the density of particles' material is constant;
- particles have the same specific heat; temperature is uniform within each particle;
- particles are inert;
- the thermal and Brownian motions of particles are neglected;
- the gravity and buoyancy forces acting on particles are neglected;
- the effect of particles' wakes is neglected;
- momentum and heat transfer are taken into account only between the gas and particles.

Under these conditions, the basic equations governing dusty-gas motion can be expressed as the conservation laws of mass, momentum and energy for each phase:

$$\frac{\partial \boldsymbol{U}_g}{\partial t} + \frac{\partial \boldsymbol{F}_g}{\partial x} = -I \ , \tag{1}$$

$$\frac{\partial \boldsymbol{U}_d}{\partial t} + \frac{\partial \boldsymbol{F}_d}{\partial x} = I \ , \tag{2}$$

where

$$\boldsymbol{U}_g = \begin{pmatrix} \rho \\ \rho u \\ E \end{pmatrix}, \quad \boldsymbol{F}_g = \begin{pmatrix} \rho u \\ \rho u^2 + p \\ (E+p)u \end{pmatrix}, \tag{3}$$

$$\boldsymbol{U}_d = \begin{pmatrix} \sigma \\ \sigma u_d \\ \Omega \end{pmatrix}, \quad \boldsymbol{F}_d = \begin{pmatrix} \sigma u_d \\ \sigma u_d^2 \\ \Omega u_d \end{pmatrix}, \tag{4}$$

$$\boldsymbol{I} = \frac{\sigma}{m} \begin{pmatrix} 0 \\ D \\ Q + u_d D \end{pmatrix}, \tag{5}$$

and E and Ω are the total energies per unit volume of the gas and particles, respectively. They are expressed as

$$E = \rho \left(C_v T + \frac{1}{2} u^2 \right) \ , \tag{6}$$

$$\Omega = \sigma \left(C_m \Theta + \frac{1}{2} u_d^2 \right) \ . \tag{7}$$

The variables ρ, u, p and T represent the density, velocity, pressure and temperature of the gas, respectively, while σ, u_d, Θ are the density, velocity and temperature of the dust particles; m is the mass of a single particle, D is the drag force acting on a single particle; C_v, C_m and Q are the specific heat of the gas at constant volume, the specific heat of the particle material and the heat transfer rate per particle, respectively.

The equation of state for a perfect gas with the gas constant R is expressed as

$$p = \rho R T \ . \tag{8}$$

The drag force D and the heat transfer rate Q are expressed via the drag coefficient C_D and the Nusselt number Nu as

$$D = \frac{1}{8} \pi d^2 \rho \left(u - u_d \right) \left| u - u_d \right| C_D \ , \tag{9}$$

$$Q = \frac{\pi d \mu C_p}{\mathrm{Pr}} \left(T - \Theta \right) \mathrm{Nu} \ , \tag{10}$$

where d is the particle diameter, C_p is the specific heat of the gas at constant pressure. The drag coefficient C_D and the Nusselt number Nu depend on the particle Reynolds number Re. The following formulas obtained by Gilbert et al. (1955) and Knudsen and Katz (1958) are adopted:

$$C_D = 0.48 + 28(\mathrm{Re})^{-0.85} \ , \tag{11}$$

$$\mathrm{Nu} = 2.0 + 0.6(\mathrm{Pr})^{1/3}(\mathrm{Re})^{1/2} \ , \tag{12}$$

where the particle Reynolds number is defined as

$$\mathrm{Re} = \frac{\rho \, d \left| u - u_d \right|}{\mu} \ . \tag{13}$$

In this study, it is assumed that the viscosity coefficient and the heat transfer rate depend only on temperature. The following formula by Chapman and Cowling (1961) is used for the viscosity coefficient:

$$\mu = 1.71 \cdot 10^{-5} \left(\frac{T}{273} \right)^{0.77} \quad \left[\mathrm{N \cdot s/m^2} \right] \ . \tag{14}$$

The heat transfer rate is determined assuming that the Prandtl number of the gas is constant:

$$\mathrm{Pr} = 0.75 \ . \tag{15}$$

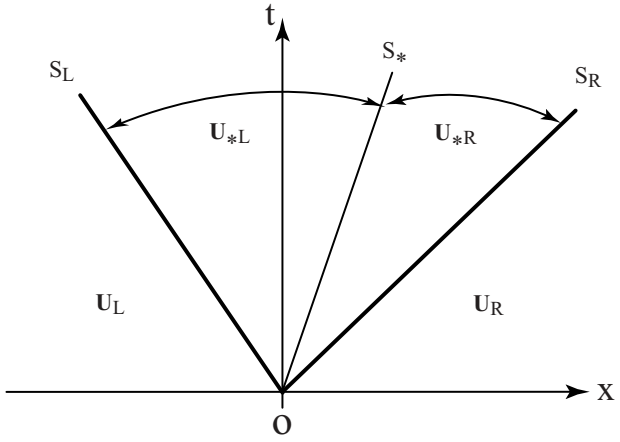

Fig. 1. Wave system of the HLLC approximate Riemann solver

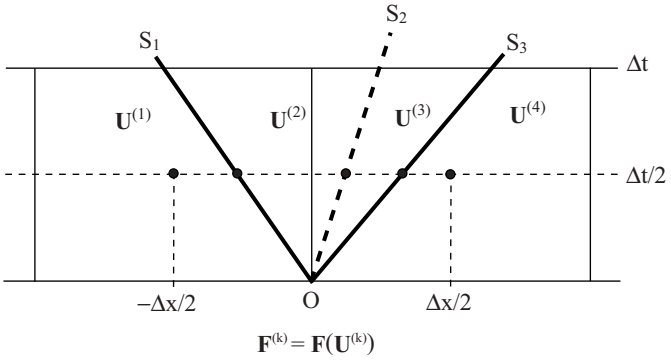

Fig. 2. Schematics of WAF numerical flux construction

2.2 Numerical methods

The terms representing the interaction between the gas and particles are the source terms in the governing Eqs. (1)–(5). These terms are handled using the operator splitting technique (Toro 1997). The governing equations are decomposed as follows:

$$\frac{\partial \boldsymbol{U}_g}{\partial t} + \frac{\partial \boldsymbol{F}_g}{\partial x} = 0 \ , \tag{16}$$

$$\frac{\partial \boldsymbol{U}_d}{\partial t} + \frac{\partial \boldsymbol{F}_d}{\partial x} = 0 \ , \tag{17}$$

$$\frac{\mathrm{d}\boldsymbol{U}_g}{\mathrm{d}t} = -\boldsymbol{I} \ , \tag{18}$$

$$\frac{\mathrm{d}\boldsymbol{U}_d}{\mathrm{d}t} = \boldsymbol{I} \ . \tag{19}$$

The solution is then obtained in two steps. The homogeneous Eqs. (16) and (17) are solved first with a second-order numerical scheme, neglecting the interaction between the phases. Let us denote this operator as $C^{(\Delta t)}$, where Δt is the time step.

Then the solutions are modified by Eqs. (18) and (19), taking into consideration the effect of the interaction. This operator is denoted as $S^{(\Delta t)}$. The ordinary differential Eqs. (18) and (19) are solved with the second order Runge-Kutta method.

To ensure the second order accuracy of the whole procedure, the following solution-update strategy from the time level n to $n+1$ is used (Strang 1968):

$$\boldsymbol{U}^{n+1} = S^{\left(\frac{1}{2}\Delta t\right)} C^{(\Delta t)} S^{\left(\frac{1}{2}\Delta t\right)} \boldsymbol{U}^n \ . \tag{20}$$

Under our assumptions, Eqs. (16) and (17) are independent and, therefore, we can use different numerical schemes for different phases.

2.2.1 Gas phase

The cell-centered finite-volume approach is used for the gas phase. The weighted average flux (WAF) method developed by Toro (1989) is employed for the calculation of numerical fluxes at the cell interfaces. The Eq. (16) is discretized as follows:

$$\boldsymbol{U}_i^{n+1} = \boldsymbol{U}_i^n + \frac{\Delta t}{\Delta x}\left[\boldsymbol{F}_{i-\frac{1}{2}} - \boldsymbol{F}_{i+\frac{1}{2}}\right] \ , \tag{21}$$

where the subscript i represents the node number; the index $i+1/2$ denotes the interface between the cells $i+1$ and i; Δx is the grid step.

The numerical flux $\boldsymbol{F}_{i+\frac{1}{2}}$ of WAF is evaluated by averaging the flux based on the Riemann problem solution at the respective interface at the time $t^n + \Delta t/2$, resulting in the second order of accuracy both in space and time:

$$\boldsymbol{F}_{i+\frac{1}{2}} = \frac{1}{\Delta x}\int_{-\frac{1}{2}\Delta x}^{\frac{1}{2}\Delta x} \boldsymbol{F}\left(\boldsymbol{U}_{i+\frac{1}{2}}\left(x, t^n + \frac{\Delta t}{2}\right)\right)\mathrm{d}x \ , \tag{22}$$

where $\boldsymbol{U}_{i+\frac{1}{2}}(x,t)$ is the Riemann problem solution with the initial data $\boldsymbol{U}_i^n$ and $\boldsymbol{U}_{i+1}^n$. The HLLC approximate Riemann problem solution (Toro 1997) is used instead of the exact solution for the sake of computational efficiency.

The HLLC Riemann problem solution consists of four states $\boldsymbol{U}^{(1)} = \boldsymbol{U}_L = \boldsymbol{U}_i^n$, $\boldsymbol{U}^{(2)} = (\boldsymbol{U}_*)_L$, $\boldsymbol{U}^{(3)} = (\boldsymbol{U}_*)_R$ and $\boldsymbol{U}^{(4)} = \boldsymbol{U}_R = \boldsymbol{U}_{i+1}^n$ divided by the three waves $S_1 = S_L$, $S_2 = S_*$ and $S_3 = S_R$ as shown in Figs. 1 and 2. As illustrated with the wave diagram in Fig. 2, the numerical flux of WAF (22) is integrated using the HLLC Riemann solution to become

$$\boldsymbol{F}_{i+\frac{1}{2}} = \frac{1}{2}(\boldsymbol{F}_i + \boldsymbol{F}_{i+1}) - \frac{1}{2}\sum_{k=1}^{3} c_k \Delta \boldsymbol{F}_{i+\frac{1}{2}}^{(k)} \ , \tag{23}$$

$$\Delta \boldsymbol{F}_{i+\frac{1}{2}}^{(k)} = \boldsymbol{F}_{i+\frac{1}{2}}^{(k+1)} - \boldsymbol{F}_{i+\frac{1}{2}}^{(k)} \ , \tag{24}$$

where c_k is the Courant number of the k-th wave expressed as

$$c_k = \frac{S_k \Delta t}{\Delta x} \quad (k = 1, 2, 3) \ , \tag{25}$$

where S_k is the speed of k-th wave.

In order to suppress numerical oscillations, the TVD condition is implemented in (23). The resulting numerical flux can be written as

$$\boldsymbol{F}_{i+\frac{1}{2}} = \frac{1}{2}(\boldsymbol{F}_i + \boldsymbol{F}_{i+1}) - \frac{1}{2}\sum_{k=1}^{3} \mathrm{sign}(c_k)\phi_{i+\frac{1}{2}}^{(k)} \Delta \boldsymbol{F}_{i+\frac{1}{2}}^{(k)} \ . \tag{26}$$

The function

$$\phi^{(k)}_{i+\frac{1}{2}} = \phi_{i+\frac{1}{2}}\left(r^{(k)}\right) \tag{27}$$

is the limiting function, and the parameter

$$r^{(k)} = \begin{cases} \dfrac{\Delta\alpha^{(k)}_{i-\frac{1}{2}}}{\Delta\alpha^{(k)}_{i+\frac{1}{2}}}\ , & \text{if} \quad c_k > 0; \\ \dfrac{\Delta\alpha^{(k)}_{i+\frac{3}{2}}}{\Delta\alpha^{(k)}_{i+\frac{1}{2}}}\ , & \text{if} \quad c_k < 0, \end{cases} \tag{28}$$

is the jump ratio of a flow variable α, typically the density.

There are several limiting functions; some of them are listed below:

SUPERBEE limiter:

$$\phi_{sa}(r,|c|) = \begin{cases} 1, & \text{if} \quad r \le 0; \\ 1-2(1-|c|)r, & \text{if} \quad 0 \le r \le 0.5; \\ |c|, & \text{if} \quad 0.5 \le r \le 1; \\ 1-(1-|c|)r, & \text{if} \quad 1 \le r \le 2; \\ 2|c|-1, & \text{if} \quad r \ge 2; \end{cases} \tag{29}$$

van Leer's limiter:

$$\phi_{vl}(r,|c|) = \begin{cases} 1, & \text{if} \quad r \le 0; \\ 1-\dfrac{(1-|c|)2r}{1+r}, & \text{if} \quad r \ge 0; \end{cases} \tag{30}$$

van Albada's limiter:

$$\phi_{va}(r,|c|) = \begin{cases} 1, & \text{if} \quad r \le 0; \\ 1-\dfrac{(1-|c|)r(1+r)}{1+r^2}, & \text{if} \quad r \ge 0; \end{cases} \tag{31}$$

MINBEE limiter:

$$\phi_{ma}(r,|c|) = \begin{cases} 1, & \text{if} \quad r \le 0; \\ 1-(1-|c|)r, & \text{if} \quad 0 \le r \le 1; \\ |c|, & \text{if} \quad r \ge 1. \end{cases} \tag{32}$$

Each function has its own merits and demerits. The choice is usually based on the stability and amount of numerical viscosity of the resulting scheme. In particular, *MINBEE* is used in this study. It introduces relatively large amount of numerical viscosity, and, accordingly, the scheme exhibits better stability, with less numerical oscillations.

The boundary conditions are set at the both ends of the calculation area using imaginary cells. Depending on the type of boundary conditions such as solid wall, inflow, outflow etc., appropriate parameter values are assigned with the standard method (Toro 1997).

2.2.2 Particle phase

The cell-centered finite-volume approach is used for calculations of the particle phase as well. Two different schemes for evaluating numerical fluxes at the cell interfaces are employed and compared in this paper. The Eq. (17) together with (4) can be rewritten in terms of the primitive variables as

$$\frac{\partial\sigma}{\partial t} + \frac{\partial(\sigma u_d)}{\partial x} = 0\ , \tag{33}$$

$$\frac{\partial u_d}{\partial t} + u_d\frac{\partial u_d}{\partial x} = 0\ , \tag{34}$$

$$\frac{\partial\Theta}{\partial t} + u_d\frac{\partial\Theta}{\partial x} = 0\ . \tag{35}$$

Let us note that Eq. (34) is Burger's equation; it has discontinuous solutions for discontinuous initial data while, in principle, there are no discontinuities propagating in the particle phase due to the assumption that the particles do not collide with each other. One way of handling this situation is to interpolate the solution between neighboring cells at the interface and avoid any solution jumps. Miura et al. (1986) used this method for calculations of the particle phase and the random choice method for the gas phase. Another opportunity is to allow overlapping of the characteristics in the Riemann problem solutions for the particle phase as done by Saurel et al. (1994). These two schemes are described and compared below.

Method 1

The vector of primitive variables $\boldsymbol{q} = (\sigma; u_d; \Theta)$ at a fixed time level, $t = 0$ for example, is linearly interpolated between two cell centers and expressed as

$$\boldsymbol{q}(x,0) = \frac{\Delta\boldsymbol{q}}{\Delta x}\,x + \boldsymbol{q}^{\circ}\ , \tag{36}$$

where $\boldsymbol{q}^{\circ}$ is its value at the cell interface ($x = 0$). For one-dimensional (1D) case and uniform grids, $\boldsymbol{q}^{\circ}$ is the arithmetic average of the cell center values. On general non-uniform grids, it is expressed using the distances dl and dr from the cell centers to the respective cell interface as

$$\boldsymbol{q}^{\circ} = \frac{\mathrm{d}r\cdot\boldsymbol{q}_l + \mathrm{d}l\cdot\boldsymbol{q}_r}{\Delta x}, \quad \Delta x = \mathrm{d}l + \mathrm{d}r. \tag{37}$$

Flow parameters at the interface $x = 0$ at an arbitrary time moment t are obtained from Eqs. (17), (36) and (37) as follows:

$$u_d = \frac{1}{1+\frac{\Delta u_d}{\Delta x}\cdot t}\,u_d^{\circ}\ , \tag{38}$$

$$\Theta = \frac{1}{1+\frac{\Delta u_d}{\Delta x}\cdot t}\left[\left\{\frac{\Delta u_d}{\Delta x}\cdot\Theta^{\circ} - \frac{\Delta\Theta}{\Delta x}\cdot u_d^{\circ}\right\}t + \Theta^{\circ}\right], \tag{39}$$

$$\sigma = \frac{1}{\left(1+\frac{\Delta u_d}{\Delta x}\cdot t\right)^2}\left[\left\{\frac{\Delta u_d}{\Delta x}\cdot\sigma^{\circ} - \frac{\Delta\sigma}{\Delta x}\cdot u_d^{\circ}\right\}t + \sigma^{\circ}\right]. \tag{40}$$

The numerical fluxes can be calculated with the primitive variables obtained from Eqs. (38)–(40) with $t = \Delta t/2$. The time step Δt is the same for the gas and particle phases.

In order to suppress numerical oscillations in the particle phase, the following *minmod* function is used to limit the gradients of primitive variables:

$$\Delta\boldsymbol{q} = \Delta\boldsymbol{q}_{i-\frac{1}{2}}\cdot\max\left\{0, \min\left(1, \Delta\boldsymbol{q}_{i+\frac{1}{2}}/\Delta\boldsymbol{q}_{i-\frac{1}{2}}\right)\right\}\ , \tag{41}$$

where

$$\Delta \boldsymbol{q}_{i+\frac{1}{2}} = \boldsymbol{q}_{i+1} - \boldsymbol{q}_i \ , \tag{42}$$

$$\Delta \boldsymbol{q}_{i-\frac{1}{2}} = \boldsymbol{q}_i - \boldsymbol{q}_{i-1} \ . \tag{43}$$

Below we refer to the method described above and the respective numerical code as "Method 1".

Method 2

The characteristic speed of the particle phase takes a single value u_d, and the solution of the Riemann problem corresponds to one of the six cases shown in Fig. 3. Figures 3a–c show the rarefaction cases in which particles from the left and right states are separated, and the solution can be written as

$$\boldsymbol{U}(x,t) = \begin{cases} \boldsymbol{U}_L, & \text{if} \quad x/t < u_d^L; \\ \boldsymbol{U}_*, & \text{if} \quad u_d^L < x/t < u_d^R; \\ \boldsymbol{U}_R, & \text{if} \quad x/t > u_d^R, \end{cases} \tag{44}$$

where the star region is vacuum:

$$\boldsymbol{U}_* = \begin{pmatrix} 0 \\ 0 \\ 0 \end{pmatrix} . \tag{45}$$

Figures 3d–f correspond to the compression, or overlapping, cases. In these cases, particles of the left and right states overlap, and the solution is expressed as follows:

$$\boldsymbol{U}(x,t) = \begin{cases} \boldsymbol{U}_L, & \text{if} \quad x/t < u_d^R; \\ \boldsymbol{U}_*, & \text{if} \quad u_d^R < x/t < u_d^L; \\ \boldsymbol{U}_R, & \text{if} \quad x/t > u_d^L, \end{cases} \tag{46}$$

where the star region is obtained by superimposing the left and right states:

$$\boldsymbol{U}_* = \begin{pmatrix} \sigma^L + \sigma^R \\ \sigma^L u_d^L + \sigma^R u_d^R \\ \Omega^L + \Omega^R \end{pmatrix} . \tag{47}$$

The Riemann problem solutions (44) and (46) are incorporated into the WAF scheme in the same way as for the gas phase. We refer to the method described in this subsection and the respective numerical code as "Method 2".

The numerical scheme for the gas phase described in Sect. 2.2.1 is the same for both Method 1 and Method 2. The time increment Δt is determined for each calculation step based on the CFL stability condition of the gas phase

$$\Delta t = C_{\mathrm{cfl}} \frac{\Delta x}{S^n_{\max}} \ , \tag{48}$$

where $C_{\mathrm{cfl}} \in (0, 1]$ is the CFL number, and $S^n_{\max}$ is the largest local characteristic speed at the time level n:

$$S^n_{\max} = \max_i \left\{ |u^n_i| + a^n_i \right\} , \tag{49}$$

where a^n_i is the sound speed of the gas at the cell i.

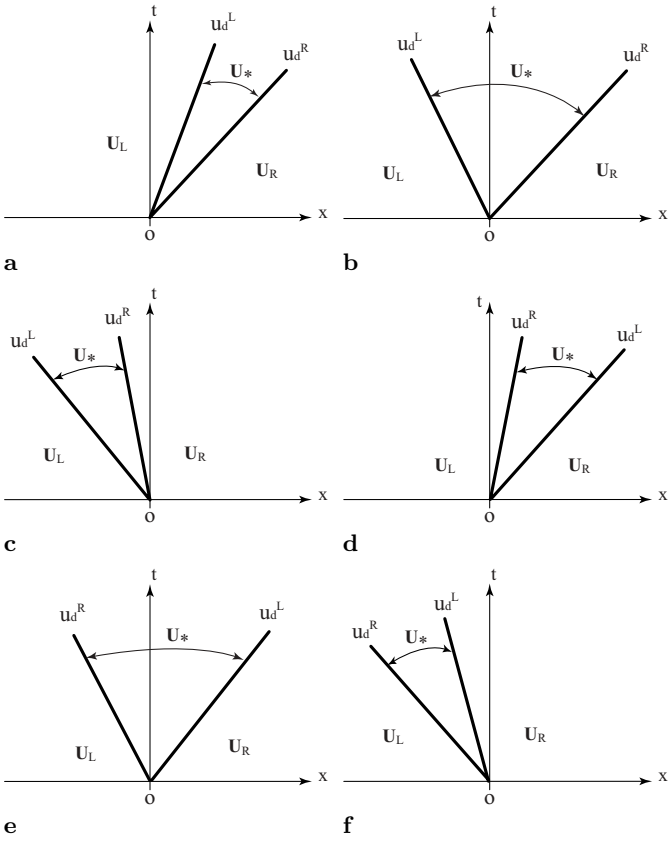

Fig. 3a–d. Six types of the Riemann problem solutions for particle flows

Table 1. Initial conditions of dusty-gas shock tube problem

		Driver gas	Test section
Pressure	(p/p_{ref})	10.0	1.0
Gas density	$(\rho/\rho_{\mathrm{ref}})$	10.0	1.0
Particle density	$(\sigma/\rho_{\mathrm{ref}})$	$1.0 \cdot 10^{-6}$	1.0
Gas velocity	(u/u_{ref})	0.0	0.0
Particle velocity	(u_d/u_{ref})	0.0	0.0

2.2.3 Comparison of the numerical schemes

Two different numerical schemes described in the previous section, Method 1 and Method 2, are compared using a dusty-gas shock tube problem. The initial conditions of the problem are listed in Table 1.

The subscript 'ref' indicates the reference state. The values p_{ref} and ρ_{ref} are assigned to be equal to the initial pressure ($p_1 = 101.3$ kPa) and density ($\rho_1 = 1.293$ kg/m^3) values of the test gas. The reference velocity u_{ref} is then obtained as

$$u_{\mathrm{ref}} = \frac{a_{f,\mathrm{ref}}}{\sqrt{\gamma}} = \sqrt{\frac{p_{\mathrm{ref}}}{\rho_{\mathrm{ref}}}} = \sqrt{\frac{p_1}{\rho_1}} \ , \tag{50}$$

where $a_{f,\mathrm{ref}}$ is the frozen sound speed of the initial state of the test gas. It is shown (Miura and Glass 1982) that

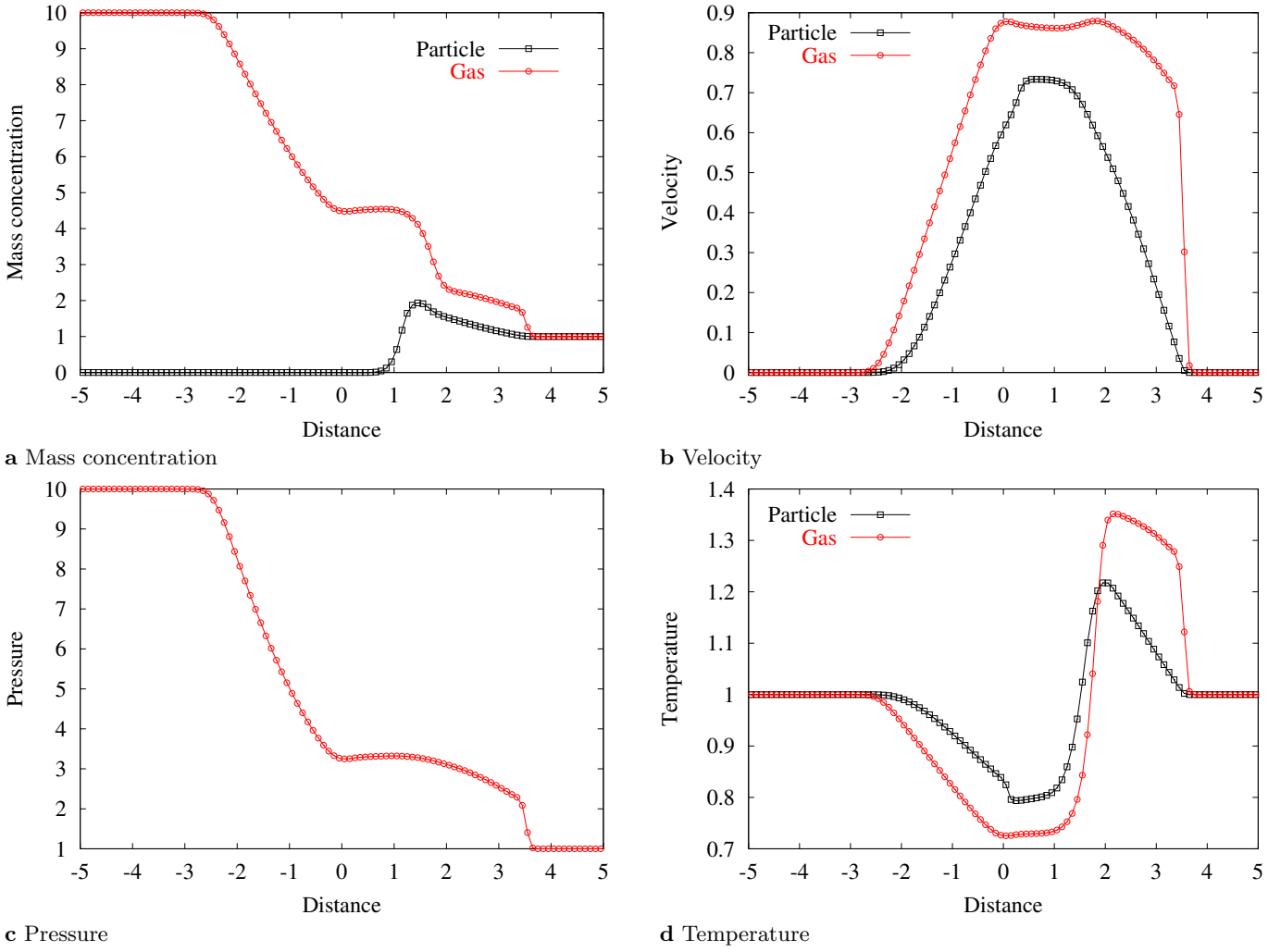

a Mass concentration **b** Velocity

c Pressure **d** Temperature

Fig. 4a–d. Dusty-gas shock tube problem solutions with Method 1

the following characteristic quantity l has the dimension of length:

$$l = \frac{8m}{\pi \rho_{\mathrm{ref}} d^2} = \frac{4}{3} \frac{\rho_p}{\rho_{\mathrm{ref}}} d = \frac{4}{3} \frac{\rho_p}{\rho_1} d, \tag{51}$$

where ρ_p is the particle material density. Here we use l as the reference length. The reference time, therefore, can be obtained as follows:

$$\tau = l / u_{\mathrm{ref}} \ . \tag{52}$$

The ratios of the mass concentrations (α) and the specific heats (β) of the solid particles and gas are both assumed to be unity:

$$\alpha = \frac{\sigma_{\mathrm{ref}}}{\rho_{\mathrm{ref}}} = 1 \ , \tag{53}$$

$$\beta = \frac{C_m}{C_v} = 1 \ . \tag{54}$$

The diameter of each dust particle is taken as 10 μm. The specific heat of crown glass ($\rho_p = 2500$ kg/m^3) is of the same order as that of air; hence, the assumption of β=1 is reasonable. Under the conditions of atmospheric pressure at room temperature, the number density of glass particles with 10μm diameter for α=1 is 0.92×10^6 cm^3. Therefore, the assumption of treating the cloud of particles as a continuum is justified. The volume ratio of the particles to the gas for α=1 is approximately 0.05%, and the assumption of neglecting the particle volume is also well justified.

The numerical results at $\tau = 20$ obtained with Method 1 and Method 2 are shown in Figs. 4 and 5, respectively. In both cases, the grid step is $\Delta x = 0.1$, and the CFL number is equal to 0.9.

It is seen in the figures that Method 1 gives, as a whole, more smooth, or diffusive, results as compared to Method 2. It should be also noted that Method 2 results in oscillations in the solid particle solution at the contact region. They are most noticeable in the plot of particle temperature distribution in Fig. 5. This instability could not be removed by lowering the CFL number as shown in Fig. 6. In fact, the results became worse as the CFL number was

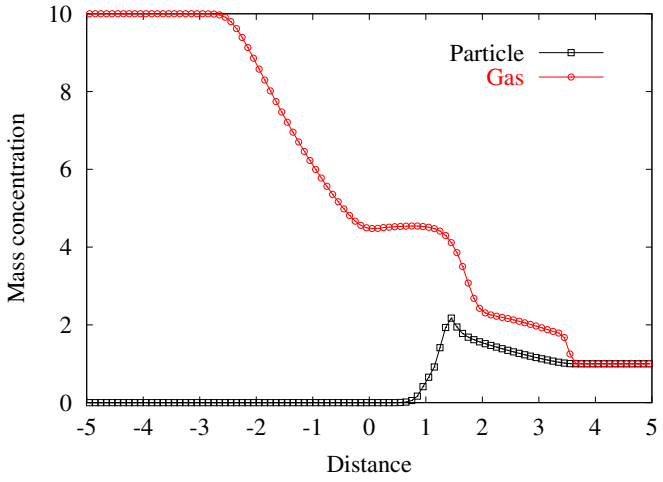

a Mass concentration

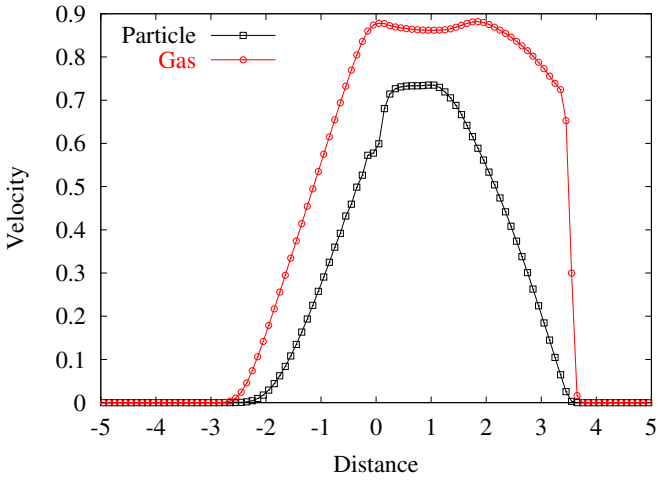

b Velocity

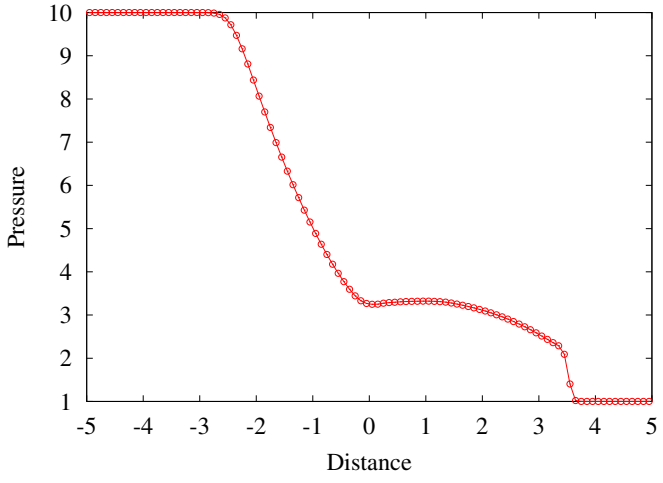

c Pressure

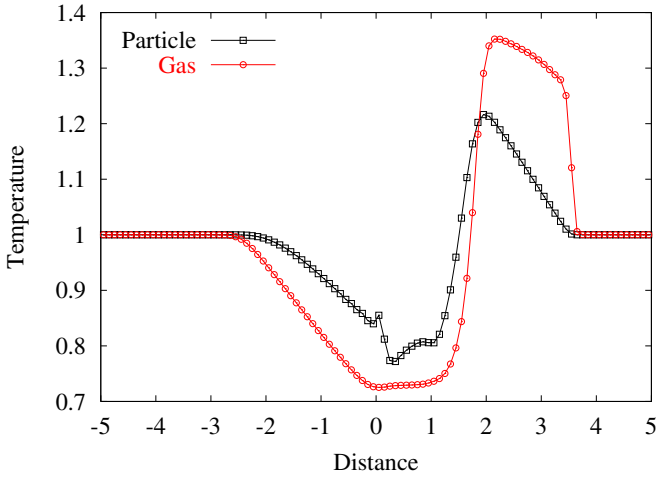

d Temperature

Fig. 5a–d. Dusty-gas shock tube problem solutions with Method 2

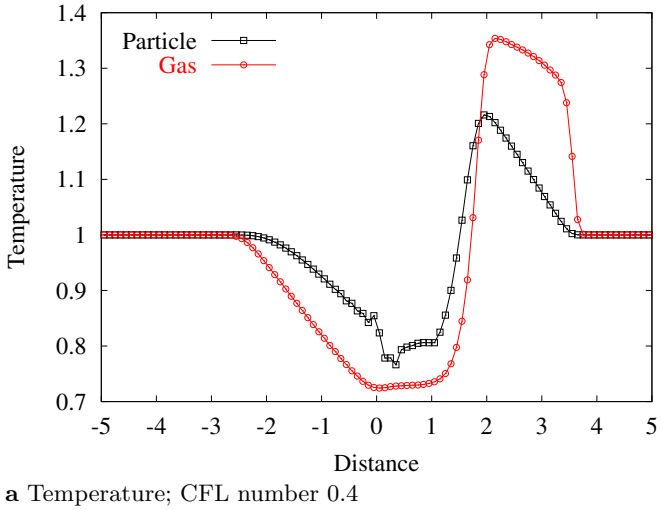

a Temperature; CFL number 0.4

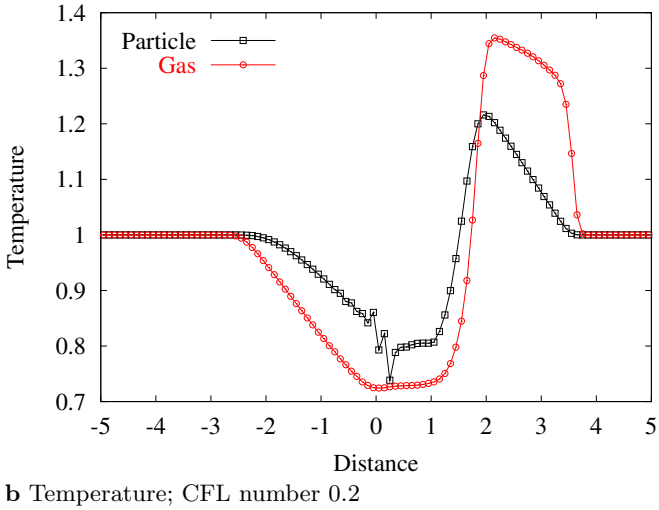

b Temperature; CFL number 0.2

Fig. 6a,b. The influence of the CFL number on the solution with Method 2

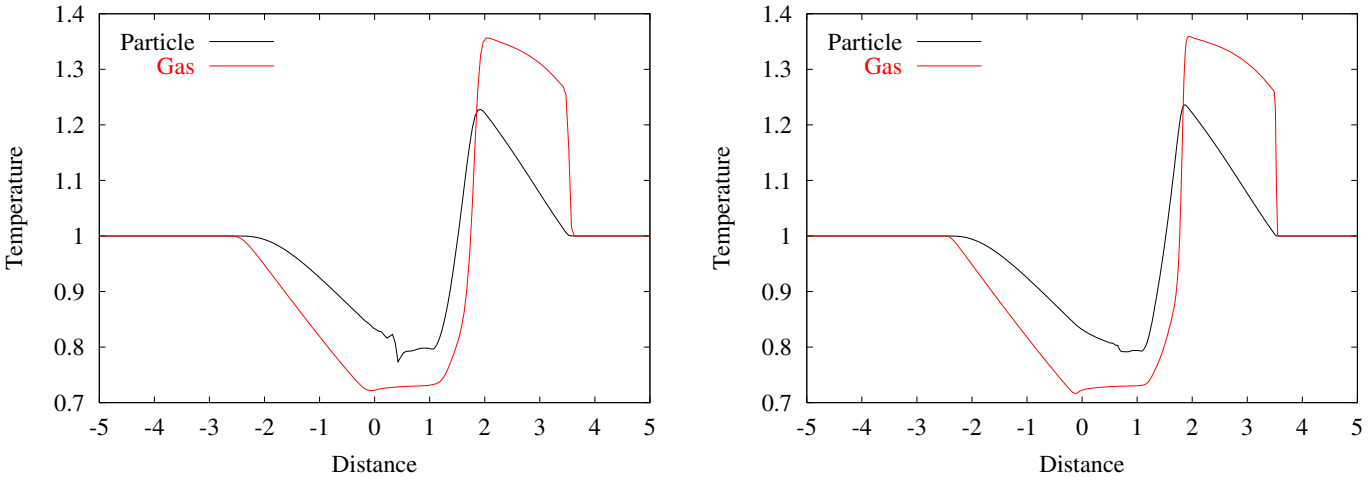

a Temperature; $\Delta x = 0.05$ **b** Temperature; $\Delta x = 0.02$

Fig. 7a,b. The effect of grid spacing on the solution with Method 2

reduced. The oscillations disappeared only when the grid step was reduced to $\Delta x = 0.02$ as shown in Fig. 7.

These observations suggest that, generally, Method 1 is preferable for calculating the particle phase. However, in order to simulate dusty gas flows with the boundary conditions allowing particle reflections from the solid wall, Method 2 is more convenient than Method 1 because it permits the existence of multiple dust-particle velocities in a numerical cell. Further investigation is required to clarify the stability issue revealed here. However, it is beyond the scope of the present study.

2.3 Shock tube problems

Two typical dusty-gas shock tube problems were calculated. The initial conditions are the same as those in Table 1 except the values of the driver gas pressure and density. The normalized pressure (p_4/p_1) and density (ρ_4/ρ_1) in the driver gas section are both either 11.5 (Case 1; partially dispersed case as explained below) or 3.46 (Case 2; fully dispersed case).

When the two phases of gas and particles are in equilibrium, the mixture can be considered as a perfect gas with the following equilibrium specific heat γ_e:

$$\gamma_e = \frac{\gamma + \alpha\beta}{1 + \alpha\beta} \ . \tag{55}$$

The equilibrium sound speed is obtained as follows (Rudinger 1964):

$$a_{1,e} = \sqrt{\frac{\gamma + \alpha\beta}{(1+\alpha)(1+\alpha\beta)} \frac{p_1}{\rho_1}} \ , \tag{56}$$

where γ is the specific heat ratio of the gas ($\gamma = 1.4$ is assumed throughout this study).

Figure 8 shows the solution of Case 1 at $\tau = 30$. The shock wave consists of a discontinuous front followed by a smooth transition region in the gas phase. Once the transition region is established behind the shock wave, the shock wave propagates at a constant speed. The frozen shock Mach number $M_{s,f}$, that is the ratio of the shock wave velocity to the sound speed of the gas in front of the shock wave, is calculated to be 1.2 in Case 1. Since the shock wave propagates with a supersonic speed relative to the gas ahead of it, it still has a sharp front, i.e. in this case we deal with a partially dispersed wave.

On the other hand, since in Case 2 the shock wave propagation mode is subsonic ($M_{s,f} = 0.9$), the shock wave is completely dispersed as shown in Fig. 9. Since the sound speed of equilibrium mixture is only 0.65 of the frozen sound speed under the current conditions ($\gamma = 1.4$, $\alpha = \beta = 1.0$), the shock Mach numbers in the mixture are more than unity in both cases.

It is worthwhile evaluating the extent of the shock transition region. By defining the transition length as the distance from the beginning of the shock transition zone to the point where the ratio u_d/u exceeds 0.99, it is found that the transition length is $6.6\,l$ in Case 1 and $35l$ for Case 2. The characteristic length l for 10 μm in diameter spheres of crown glass (density 2500 kg/m^3) is 2.6 cm. Therefore, the transition zone lengthes for Case 1 and Case 2 are 18 cm and 91 cm, respectively.

2.4 Comparison with quasi-steady solutions

Once the transition post-shock region is established, the shock wave propagates at a constant velocity and the flow can be considered as steady in the coordinate system moving with the same speed. This quasi-steady flow can be obtained numerically by integrating the following steady equations and the equation of state (8):

$$\frac{\mathrm{d}}{\mathrm{d}x}(\rho u) = 0 \ , \tag{57}$$

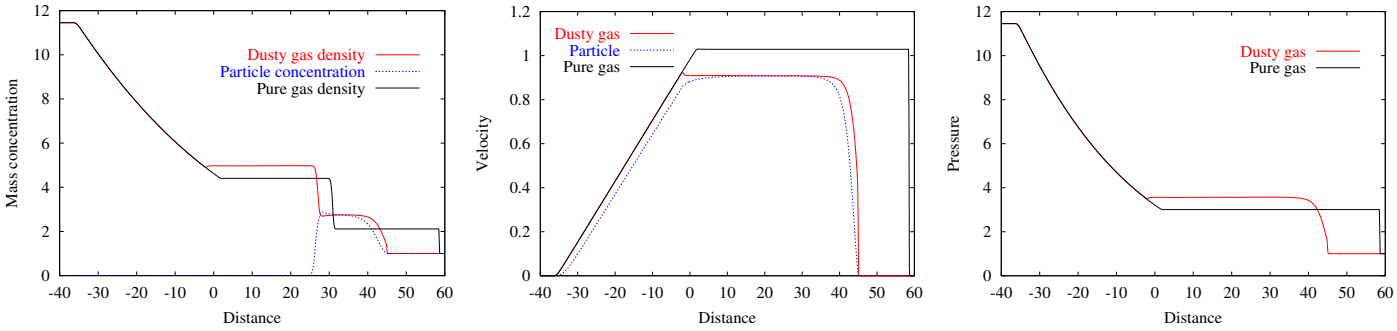

a Mass concentration **b** Velocity **c** Pressure

Fig. 8a–c. Dusty-gas shock tube problem solution; $p_4/p_1 = 11.5$; $\tau = 30$

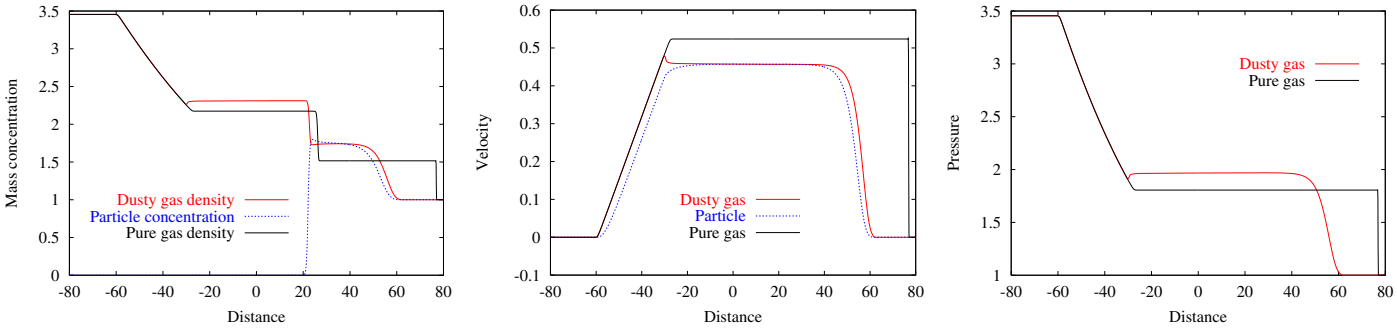

a Mass concentration **b** Velocity **c** Pressure

Fig. 9a–c. Dusty-gas shock tube problem solution; $p_4/p_1 = 3.46$; $\tau = 50$

$$\frac{\mathrm{d}}{\mathrm{d}x}\left(\sigma u_d\right) = 0 \ , \tag{58}$$

$$\frac{\mathrm{d}}{\mathrm{d}x}\left(\rho u^2 + \sigma {u_d}^2 + p\right) = 0 \ , \tag{59}$$

$$\frac{\mathrm{d}}{\mathrm{d}x}\left\{\rho u\left(C_p T + \frac{1}{2}u^2\right) + \sigma u_d\left(C_m \Theta + \frac{1}{2}{u_d}^2\right)\right\} = 0 \ , \tag{60}$$

$$\frac{\mathrm{d}u_d}{\mathrm{d}x} = \frac{D}{m u_d} \ , \tag{61}$$

$$\frac{\mathrm{d}\Theta}{\mathrm{d}x} = \frac{Q}{m C_m u_d} \ . \tag{62}$$

The shock wave profiles obtained with the quasi-steady analysis for the initial conditions used in the previous sections are compared with the previous non-steady solutions in Figs. 10 and 11.

Here the fourth-order Runge-Kutta method is used to integrate Eqs. (57) to (62). The curves obtained by the quasi-steady analysis and by the unsteady numerical simulation are indicated, respectively, as “steady” and “unsteady” in the figures.

It is seen in Fig. 10 that the discontinuous shock front spreads over two to three numerical cells as expected for the second-order shock-capturing scheme used here. The remaining portions of the profiles obtained with the two different methods agree quite well in both cases of partially and fully dispersed shock waves. This is an indication of the accuracy of the numerical code.

2.5 Drag coefficients

The drag coefficient C_D is one of the important parameters for studying dusty gas flows. The standard drag coefficient based on experimental data is known for a single spherical particle in a steady incompressible flow at a constant temperature (Soo 1967). It is represented by the following set of piecewise functions (Clift et al. 1978; Igra and Ben-Dor 1988) and shown in Fig. 12a:

$$C_D = \frac{3}{16} + \frac{24}{\mathrm{Re}}, \qquad \text{for} \quad 0 < \mathrm{Re} < 0.01; \tag{63}$$

$$\log\left(C_D \frac{\mathrm{Re}}{24} - 1\right) = -0.881 + 0.82w - 0.05w^2, \quad \text{for} \quad 0.01 < \mathrm{Re} < 20; \tag{64}$$

$$\log\left(C_D \frac{\mathrm{Re}}{24} - 1\right) = -0.7133 + 0.6305w, \quad \text{for} \quad 20 < \mathrm{Re} < 260; \tag{65}$$

$$\log\left(C_D\right) = 1.6435 - 1.1242w + 0.1558w^2, \quad \text{for} \quad 260 < \mathrm{Re} < 1.50 \cdot 10^3; \tag{66}$$

$$\log\left(C_D\right) = -2.4571 + 2.5558w - 0.9295w^2 + 0.1049w^3, \quad \text{for} \quad 1.50 \cdot 10^3 < \mathrm{Re} < 1.20 \cdot 10^4; \tag{67}$$

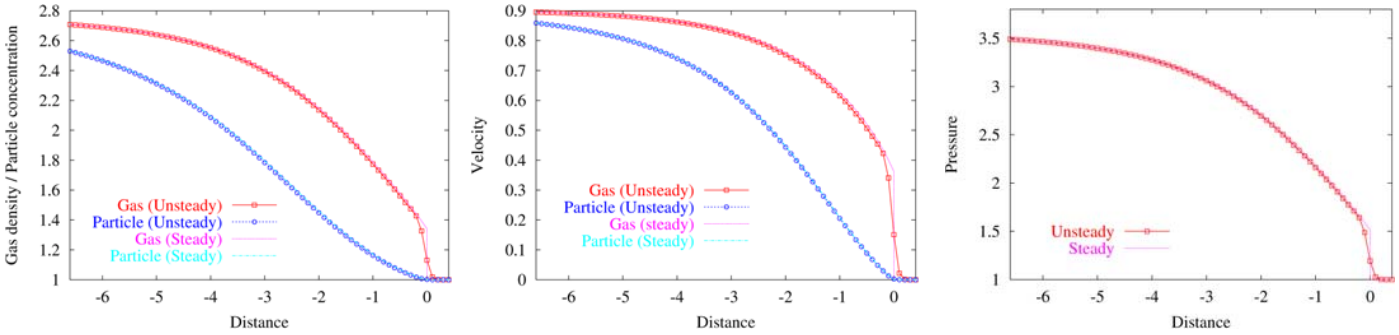

a Mass concentration **b** Velocity **c** Pressure

Fig. 10a–c. Quasi-steady shock profiles; $M_{s,f} = 1.2$

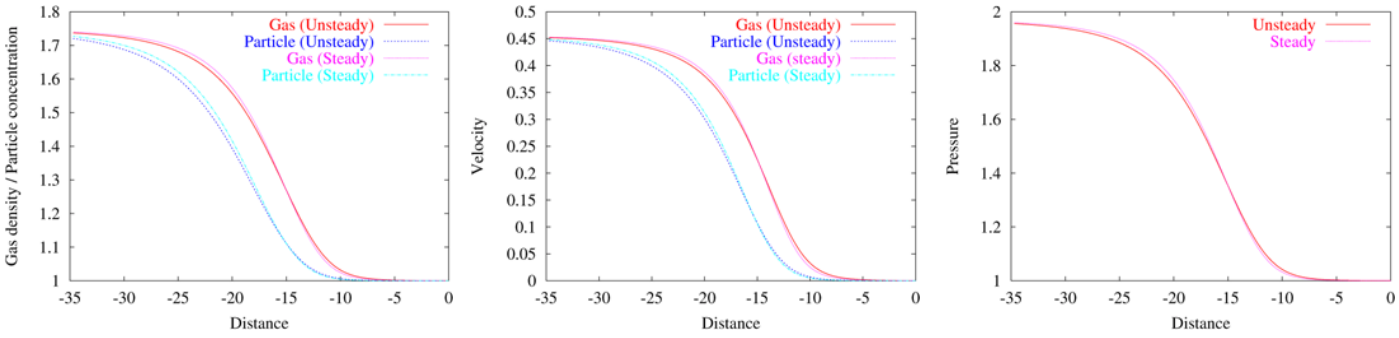

a Mass concentration **b** Velocity **c** Pressure

Fig. 11a–c. Quasi-steady shock profiles; $M_{s,f} = 0.9$

$$\log(C_D) = -1.9181 + 0.6370w - 0.0636w^2, \quad \text{for} \quad 1.20 \cdot 10^4 < \mathrm{Re} < 4.40 \cdot 10^4; \tag{68}$$

$$\log(C_D) = -4.3390 + 1.5809w - 0.1546w^2, \quad \text{for} \quad 4.40 \cdot 10^4 < \mathrm{Re} < 3.38 \cdot 10^5; \tag{69}$$

$$C_D = 29.78 - 5.3w, \quad \text{for} \quad 3.38 \cdot 10^5 < \mathrm{Re} < 4.03 \cdot 10^5; \tag{70}$$

$$C_D = -0.49 + 0.1w, \quad \text{for} \quad 4.03 \cdot 10^5 < \mathrm{Re} < 10^6; \tag{71}$$

$$C_D = 0.19 - \frac{8 \cdot 10^4}{\mathrm{Re}}, \quad \text{for} \quad 10^6 < \mathrm{Re} < 10^8, \tag{72}$$

where

$$w = \log_{10}(\mathrm{Re}). \tag{73}$$

Also shown in Fig. 12a are the early models by Newton, Stokes and Oseen which are cited by Soo (1976) as

$$\text{Newton} \qquad C_D = 0.44\ ; \tag{74}$$

$$\text{Stokes} \qquad C_D = \frac{24}{\mathrm{Re}}\ ; \tag{75}$$

$$\text{Oseen} \qquad C_D = \frac{24}{\mathrm{Re}}\left(1 + \frac{3}{16}\mathrm{Re}\right)\ . \tag{76}$$

Figure 12a shows that the drag coefficients of Stokes and Oseen agree with the standard drag coefficient for the Reynolds number up to unity while Newton's drag coefficient matches well with the standard one in the range from $\mathrm{Re} \sim 1000$ up to the critical Reynolds number ($2 \sim 4{\cdot}10^5$).

Several approximations to the standard drag coefficient were proposed in the past. Klyachko suggested the following drag coefficient (Fuchs 1964):

$$C_D = \frac{24}{\mathrm{Re}}\left(1 + \frac{(\mathrm{Re})^{2/3}}{6}\right)\ , \tag{77}$$

which well represents the standard coefficient in the range $\mathrm{Re} < 1000$. Gilbert et al. (1955) approximated the standard coefficient below the critical Reynolds number by the following formula:

$$C_D = 0.48 + 28(\mathrm{Re})^{-0.85}\ . \tag{78}$$

Clift et al. (1978) introduced the approximation with the following piecewise functions:

$$C_D = \begin{cases} \dfrac{24}{\mathrm{Re}}\left(1 + 0.15(\mathrm{Re})^{0.687}\right), & \text{for} \quad 0 < \mathrm{Re} < 800; \\ \dfrac{24}{\mathrm{Re}}\left(1 + 0.15(\mathrm{Re})^{0.687}\right) + \dfrac{0.42}{1 + 42500(\mathrm{Re})^{-1.16}}, & \text{for} \quad 800 < \mathrm{Re} < 3 \cdot 10^5 \end{cases} \tag{79}$$

Figure 12b shows the above approximate formulas in comparison with the standard coefficient. It is seen that

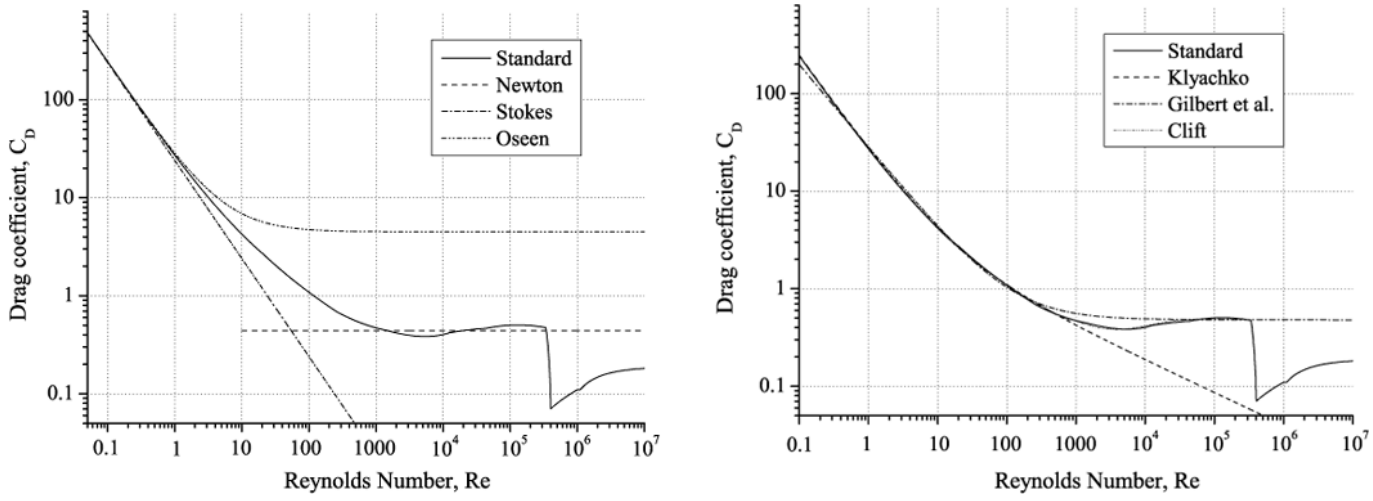

a **b**

Fig. 12a,b. Drag coefficient of a sphere vs. the particle Reynolds number. **a** Curves for the standard drag coefficient and the Newton, Stokes and Oseen drag coefficients; **b** approximations to the standard drag coefficient

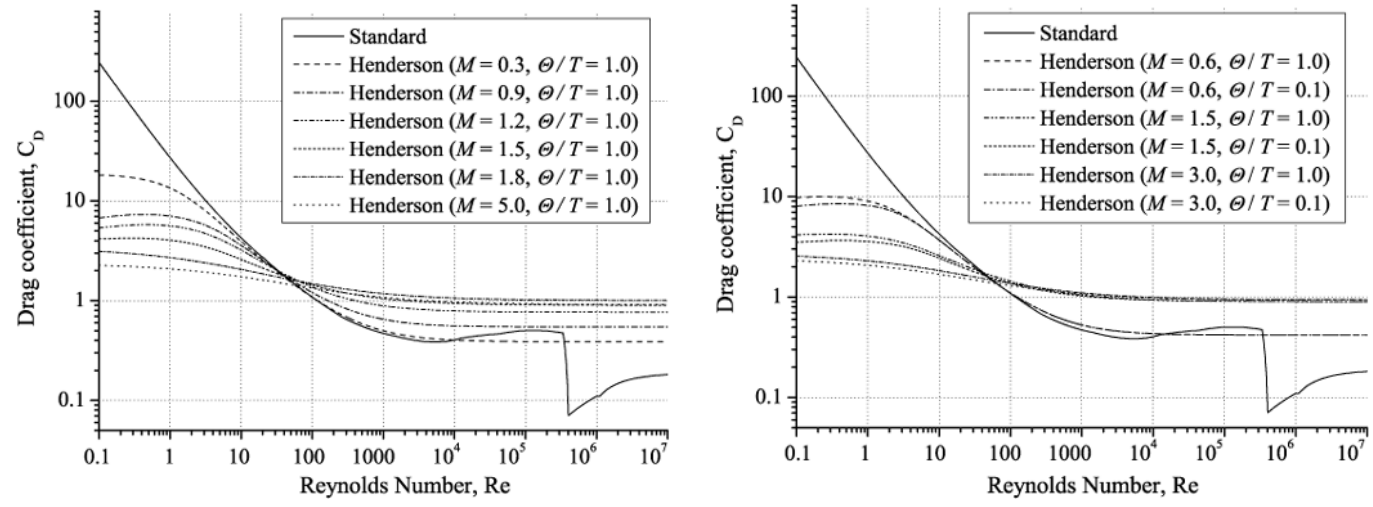

a C_D for different Mach numbers **b** C_D for different temperatures

Fig. 13a,b. Henderson's drag coefficient C_D vs. the particle Reynolds number

the drag coefficient of Clift et al. (1978) agrees with the standard drag coefficient very well. The formula proposed by Gilbert et al. (1955) is an attractive alternative because of its simplicity. This is considered to be an advantage for numerical simulations.

While all previous models were obtained for incompressible flows, Henderson (1976) proposed the following drag coefficient taking into account compressibility and the temperature difference between the solid particles and gas. In the subsonic region ($M \leq 1.0$), it is

$$C_D = \frac{24}{\mathrm{Re} + \mathrm{S}\left\{4.33 + \frac{3.65-1.53\Theta/\mathrm{T}}{1+0.353\Theta/\mathrm{T}} \exp\left(-0.247\frac{\mathrm{Re}}{\mathrm{S}}\right)\right\}}$$

$$+ \exp\left(-0.5\frac{M}{\sqrt{\mathrm{Re}}}\right)\left\{\frac{4.5 + 0.38\left(0.03\mathrm{Re} + 0.48\sqrt{\mathrm{Re}}\right)}{1 + 0.03\mathrm{Re} + 0.48\sqrt{\mathrm{Re}}}\right.$$

$$\left. +0.1M^2 + 0.2M^8\right\} + 0.6S\left\{1 - \exp\left(-\frac{M}{\mathrm{Re}}\right)\right\}, \quad (80)$$

and for $M \geq 1.75$

$$C_D = \frac{0.9 + \frac{0.34}{M^2} + 1.86\sqrt{\frac{M}{\mathrm{Re}}}\left(2 + \frac{2}{S^2} + \frac{1.058}{S}\sqrt{\frac{\Theta}{T}} - \frac{1}{S^4}\right)}{1 + 1.86\sqrt{\frac{M}{\mathrm{Re}}}}, \quad (81)$$

where

$$S = M\sqrt{\frac{\gamma}{2}}\,. \quad (82)$$

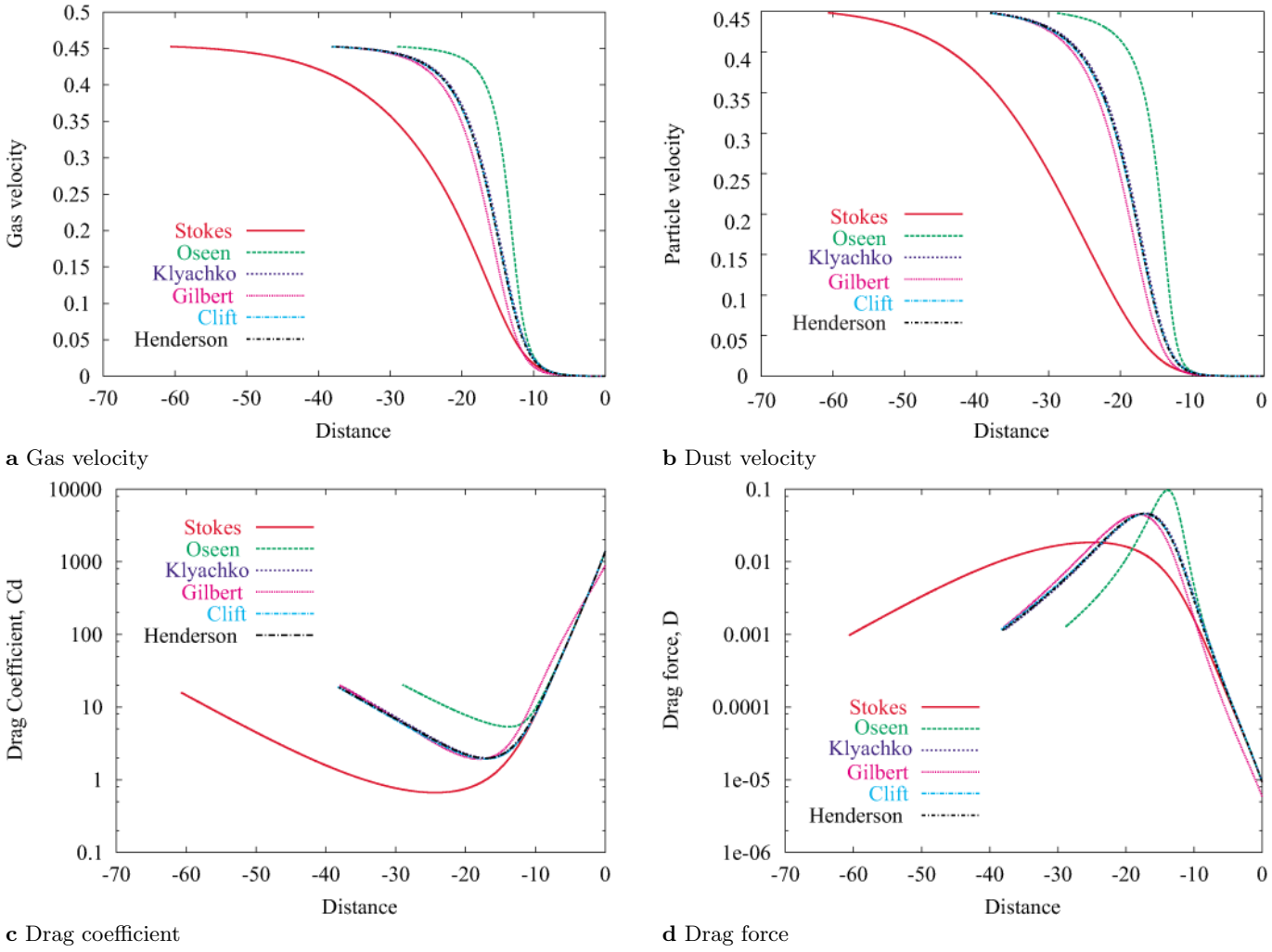

a Gas velocity **b** Dust velocity

c Drag coefficient **d** Drag force

Fig. 14a–d. Quasi-steady solutions with different drag coefficients; $M_{s,f} = 0.9$

The drag coefficient in between $(1.0 < M < 1.75)$ is given by the following linear interpolation formula:

$$C_D = C_D|_{M=1.0} + \frac{4}{3}(M - 1.0)\left(C_D|_{M=1.75} - C_D|_{M=1.0}\right) , \tag{83}$$

where $C_D|_{M=1.0}$ is the value of C_D obtained by substituting $M = 1.0$ in Eq. (80) while $C_D|_{M=1.75}$ is from Eq. (81) with $M = 1.75$.

Figure 13 shows the dependence of Henderson's drag coefficient from the particle Reynolds number. For the Reynolds number $\mathrm{Re} > 100$, Henderson's drag coefficient increases for $M < 1.75$ and decreases for $M > 1.75$. For $\mathrm{Re} < 100$, it decreases with increasing the Mach number M. As to the temperature dependence, the drag coefficient decreases with decreasing the solid-particles-to-gas temperature ratio Θ/T, though the effect is small.

For a cloud of solid particles, it is expected that the drag coefficient should be different from that of a single particle due to interactions between the particles and the disturbances or wakes generated by them. Ingebo (Rudinger 1970) experimentally obtained the following drag coefficient for a cloud of particles:

$$C_D = \frac{27}{(\mathrm{Re})^{0.84}} , \quad \text{for} \quad 6 < \mathrm{Re} < 400 . \tag{84}$$

This shows that the drag coefficient decreases rapidly with increasing the Reynolds number. Rudinger also obtained the following formula for the drag coefficient from shock tube experiments:

$$C_D = \frac{6000}{(\mathrm{Re})^{1.7}} , \quad \text{for} \quad 50 < \mathrm{Re} < 300 . \tag{85}$$

It also shows rapid decrease of the drag coefficient with increasing the Reynolds number.

In addition to the effects of compressibility and temperature differences, the flow unsteadiness is also considered to be important for transient flows. Quite a few papers on the unsteady drag coefficient have been published so far (Igra and Takayama 1991; Falcovitz and Igra 2000; Devals et al. 2003). Several correlations for the drag coefficient of a sphere in unsteady flow have been proposed.

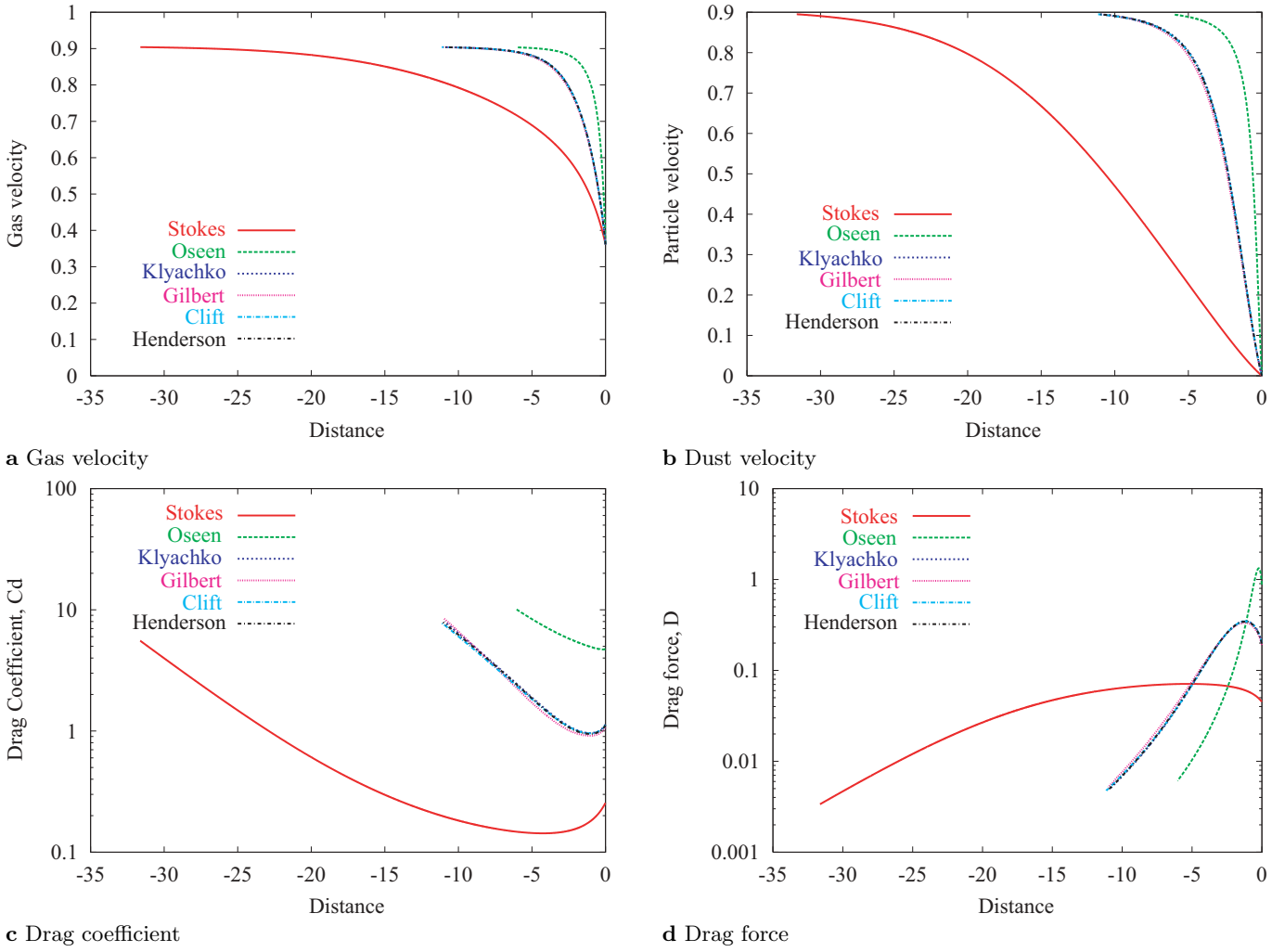

a Gas velocity **b** Dust velocity

c Drag coefficient **d** Drag force

Fig. 15a–d. Quasi-steady solutions with different drag coefficients; $M_{s,f} = 1.2$

Some of them seem to give better agreement with experimental data than others. However, there are still some issues to be clarified. The experimental and numerical studies of the unsteady drag coefficient are now being carried out at our laboratory.

In the present paper, the shock wave profiles are calculated using the quasi-steady analysis with the following six drag coefficients: Stokes (75), Oseen (76), Klyachko (77), Gilbert (78), Clift (79), and Henderson (80)∼(83).

Figure 14 shows the results for the frozen shock Mach number $M_{s,f} = 0.9$ which corresponds to the case of fully dispersed shock front. In this case, the Reynolds number ranges up to about 40. The drag coefficients of Stokes and Oseen give quite different results from the approximate formulas of the standard drag coefficient by Klyachko, Gilbert, Clift, and Henderson. The models of Stokes and Oseen show completely different transition lengths even for this case of relatively low Reynolds number flow. The other four models give almost the same drag coefficients in this Reynolds number range. The shock wave profiles accordingly are almost identical.

Figure 15 shows the results for the frozen shock Mach number $M_{s,f} = 1.2$ which corresponds to the case of partially dispersed shock front. In this case, the Reynolds number goes up to around 200. The results of the models of Stokes and Oseen are quite different from those produced by other models. The differences are much more pronounced as compared to the previous case. The Stokes model leads to several times larger transient distances, while the model of Oseen gives almost one-half what is expected from the standard drag coefficient. In this case, again, the other four models do not show significant differences among themselves.

Figure 16 shows the results for the frozen shock Mach number $M_{s,f} = 3.0$ which also corresponds to the case of partially dispersed shock front. In this case, the Reynolds number ranges up to 1000 and, needless to say, the models of Stokes and Oseen give completely different (wrong) results. As to other models, although there are notable differences in their values of the drag coefficient, the shock profiles calculated with them are still quite similar. The model of Henderson gives a noticeable peak at the shock

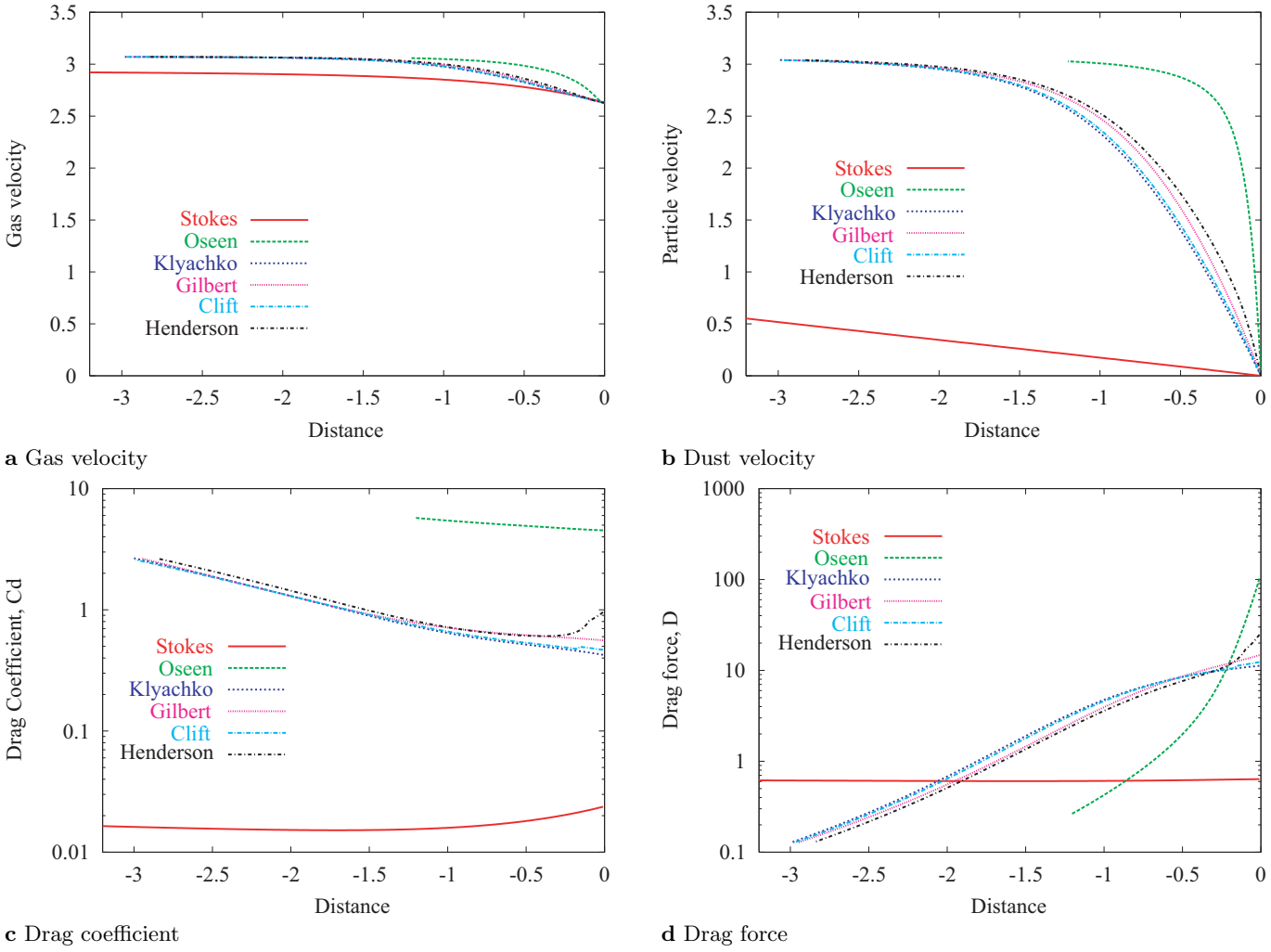

a Gas velocity **b** Dust velocity

c Drag coefficient **d** Drag force

Fig. 16a–d. Quasi-steady solutions with different drag coefficients; $M_{s,f} = 3.0$

front. However, its influence appears to be localized and the shock profiles, as a whole, are quite similar to those obtained from other models.

Within the Reynolds number range considered in our study, all models tested provide similar results, except for the models of Stokes and Oseen. These two models are valid only for very small Reynolds numbers (Re $<$ 1) which are completely out of the range of current interest, and the large deviations from the other models were expected. On the other hand, it is seen that the differences in the numerical results among the Klyachko (77), Gilbert (78), Clift (79) and Henderson (80)∼(83) approximations are very small despite the fact that the model complexity differs very much from one model to another. Considering the fact that those models are not fully established, especially for the cloud of dust particles, the choice of a model must be made wisely, considering computational efficiency and the prospective applications. In the current study, the drag coefficient model of Gilbert was used extensively due to its simplicity and, hence, computational efficiency.

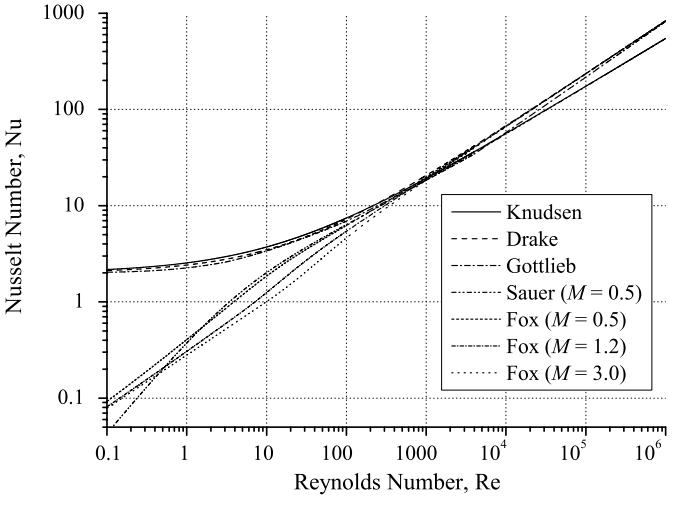

Fig. 17. Nusselt number Nu vs. the particle Reynolds number

2.6 Nusselt number

The heat transfer rate for a solid particle immersed into a steady flow depends on the local flow velocity and temperature. Knudsen and Katz (1958) proposed the following formula for the Nusselt number as a function of the Reynolds and Prandtl numbers:

$$\mathrm{Nu} = 2 + 0.6(\mathrm{Pr})^{1/3}(\mathrm{Re})^{1/2} \ , \tag{86}$$

where the definitions of the Nusselt and Prandtl numbers are

$$\mathrm{Nu} = \frac{d \cdot h}{\kappa}, \qquad \mathrm{Pr} = \frac{\mu C_p}{\kappa} \ ,$$

where h and κ are the heat-transfer rate and the heat conduction coefficient of the fluid. The model (86) is used extensively in this study. There have been many other mathematical models proposed and the effect of adopting different models is investigated in this section.

Drake (1961) suggested the following formula which is similar to Knudsen and Katz's model:

$$\begin{aligned} &\mathrm{Nu} = 2 + 0.459(\mathrm{Pr})^{0.33}(\mathrm{Re})^{0.55}, \\ &\text{for} \quad 1 < \mathrm{Re} < 7000, \ \ 0.6 < \mathrm{Pr} < 400 \ . \end{aligned} \tag{87}$$

Gottlieb and Coskunses (1985) proposed the following model for the Nusselt number in the air:

$$\mathrm{Nu} = \begin{cases} 1 + (1 + \mathrm{Re})^{1/3}, & \text{for } 0 \le \mathrm{Re} < 3; \\ 1 + (1 + 0.70\mathrm{Re})^{1/3}(\mathrm{Re})^{0.077}, & \text{for } 3 < \mathrm{Re} < 100; \\ 1 + 0.6777(\mathrm{Re})^{0.47}, & \text{for } 100 < \mathrm{Re} < 4000; \\ 1 + 0.272(\mathrm{Re})^{0.58}, & \text{for } 4000 < \mathrm{Re} < 10^6. \end{cases} \tag{88}$$

Sauer (1951) suggested to account for the effect of compressibility in subsonic flows as follows:

$$\mathrm{Nu} = \frac{\mathrm{Nu}^0}{1 + 3.42\frac{M}{\mathrm{RePr}}\mathrm{Nu}^0} \ , \quad \text{for } \ \le M \le 1, \tag{89}$$

where Nu^0 represents the Nusselt number obtained from an incompressible model. Another compressible model has been developed by Fox et al. (1978):

$$\mathrm{Nu} = \frac{2\exp(-M)}{1 + 17\frac{M}{\mathrm{Re}}} + 0.459(\mathrm{Pr})^{0.33}(\mathrm{Re})^{0.55} \times$$

$$\frac{1 + 0.5\exp\left(-17\frac{M}{\mathrm{Re}}\right)}{1.5} \ , \quad \text{for } \mathrm{Re} \le 10^4, \ M < 6 \ . \tag{90}$$

In Fig. 17, the Nusselt number approximations are plotted as functions of the Reynolds number at a fixed value of the Prandtl number (Pr = 0.75). It is seen that there are two groups of curves. One group corresponds to the incompressible models (86)–(88) while another – to the compressible models (89), (90). Almost all curves give more or less the same Nusselt number of 20 at the Reynolds number of 1000; see Fig. 20c. At low Reynolds numbers, the compressible models result in smaller values as compared to those from the incompressible ones, and the difference is larger for smaller Reynolds numbers. On the contrary, the values of the compressible models are larger for the Reynolds numbers Re > 1000.

The effect of differences in the Nusselt number models on the shock wave profiles is shown in Figs. 18–20. The figures are obtained with the quasi-steady analysis using the Nusselt number models (86)–(90).

Figure 18 shows the shock profiles for the frozen shock Mach number $M_{s,f} = 0.9$ corresponding to the fully dispersed shock wave case. In this case, all the models give similar shock profiles in spite of noticeable differences in the Nusselt numbers themselves. Since the Reynolds number is less than 30, the Fox model leads to the lowest Nusselt number and the temperature rise in the particle phase behind the shock is most gradual. However, only minor differences are observed in the transition length.

Figure 19 depicts the shock profiles for the frozen shock Mach number $M_{s,f} = 1.2$ representing the partially dispersed shock wave case. All the models except for the Fox model give similar profiles. Figure 20 illustrates the shock profiles for the frozen shock Mach number $M_{s,f} = 3.0$. It is seen that the Fox model differs even more from the others. Let us notice that the gas temperature has a maximum in the transition region. The fact that the results of the Fox model are noticeably different does not mean that the model is inferior to the others. This simply means that the evaluation of the models must be carried out by comparing them with precise experimental data obtained under unsteady conditions.

3 Two-dimensional dusty-gas flows

The numerical code developed and evaluated in the previous section was extended to two-dimensional (2D) problems. Oblique shock reflections in a dusty gas were simulated, and the results are shown below and discussed mainly in the light of inherently non-selfsimilar nature of the flows.

3.1 Basic equations and numerical method

The governing equations of the dusty gas flows in two spatial dimensions can be written as:

$$\frac{\partial \boldsymbol{U}_g}{\partial t} + \frac{\partial \boldsymbol{F}_g}{\partial x} + \frac{\partial \boldsymbol{G}_g}{\partial y} = -\boldsymbol{I} \ , \tag{91}$$

$$\frac{\partial \boldsymbol{U}_d}{\partial t} + \frac{\partial \boldsymbol{F}_d}{\partial x} + \frac{\partial \boldsymbol{G}_d}{\partial y} = \boldsymbol{I} \ , \tag{92}$$

where the vectors of conserved quantities and fluxes for the gas phase are

$$\boldsymbol{U}_g = \begin{pmatrix} \rho \\ \rho u \\ \rho v \\ E \end{pmatrix}, \boldsymbol{F}_g = \begin{pmatrix} \rho \\ \rho u \\ \rho v \\ E \end{pmatrix}, \boldsymbol{G}_g = \begin{pmatrix} \rho v \\ \rho uv \\ \rho v^2 + p \\ (E + p)v \end{pmatrix}, \tag{93}$$

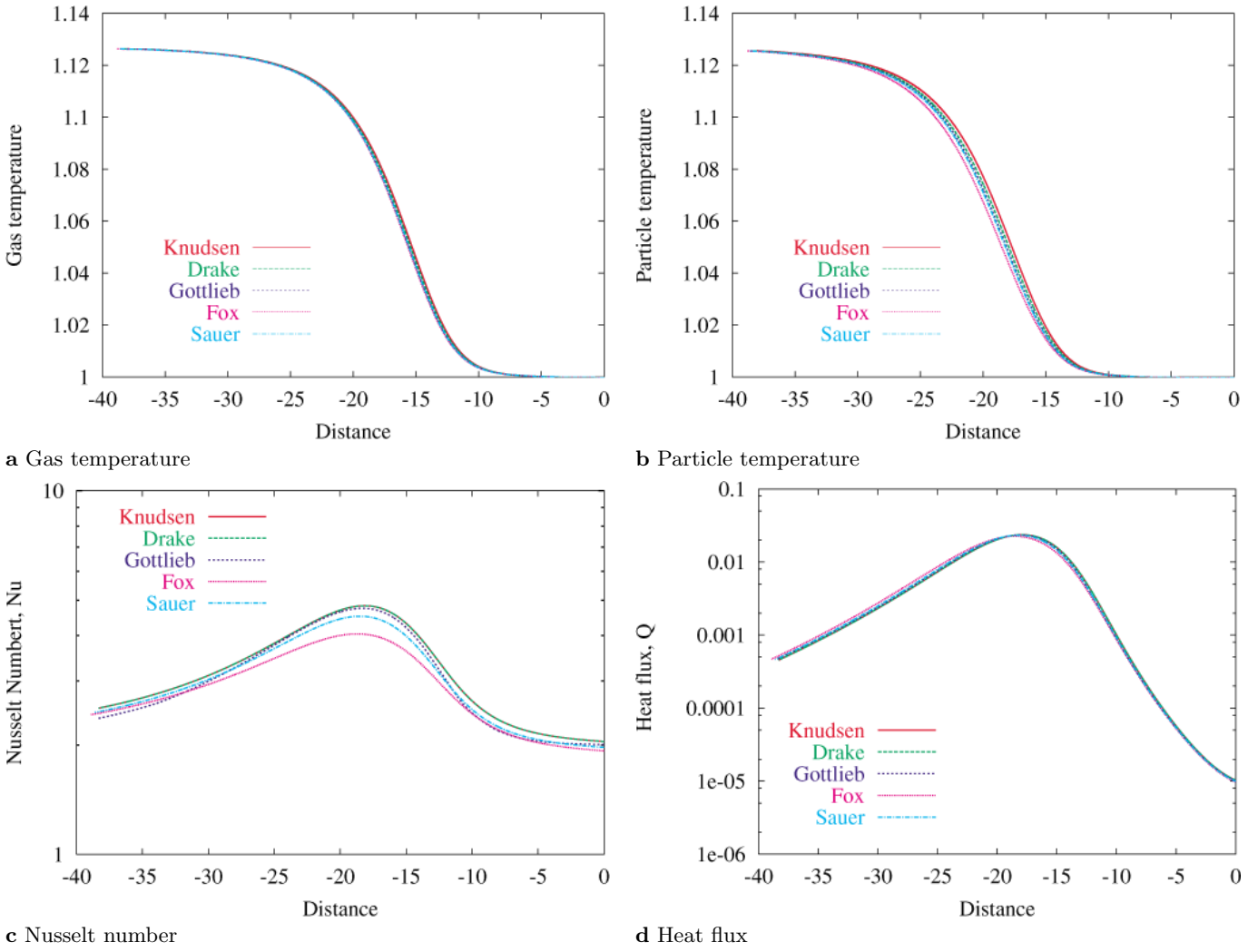

a Gas temperature **b** Particle temperature

c Nusselt number **d** Heat flux

Fig. 18a–d. Effect of different Nusselt number models; $M_{s,f} = 0.9$

and for the solid particle phase are

$$\boldsymbol{U}_d = \begin{pmatrix} \sigma \\ \sigma u_d \\ \sigma v_d \\ \Omega \end{pmatrix}, \quad \boldsymbol{F}_d = \begin{pmatrix} \sigma u_d \\ \sigma {u_d}^2 \\ \sigma u_d v_d \\ \Omega u_d \end{pmatrix}, \quad \boldsymbol{G}_d = \begin{pmatrix} \sigma u_d \\ \sigma u_d v_d \\ \sigma {v_d}^2 \\ \Omega v_d \end{pmatrix}. \tag{94}$$

The vector of phase interaction terms is

$$\boldsymbol{I} = \frac{\sigma}{m} \begin{pmatrix} 0 \\ D_x \\ D_y \\ Q + u_d D_x + v_d D_y \end{pmatrix}. \tag{95}$$

The total energies of the gas and particles are

$$E = \rho \left\{ C_v T + \frac{1}{2} \left(u^2 + v^2 \right) \right\}, \tag{96}$$

$$\Omega = \sigma \left\{ C_m \Theta + \frac{1}{2} \left({u_d}^2 + {v_d}^2 \right) \right\}, \tag{97}$$

where u and u_d are the x-components of gas and dust velocities and v and v_d are the y-components. The x and y-components of the Drag force are given as:

$$D_x = \frac{1}{8} \pi d^2 \rho \left(u - u_d \right) \sqrt{(u - u_d)^2 + (v - v_d)^2}\, C_D, \tag{98}$$

$$D_y = \frac{1}{8} \pi d^2 \rho \left(v - v_d \right) \sqrt{(u - u_d)^2 + (v - v_d)^2}\, C_D. \tag{99}$$

As in the 1D case, the following models of the drag coefficient and the Nusselt number are assumed:

$$C_D = 0.48 + 28(\mathrm{Re})^{-0.85}, \tag{100}$$

$$\mathrm{Nu} = 2.0 + 0.6(\mathrm{Pr})^{1/3}(\mathrm{Re})^{1/2}. \tag{101}$$

The particle Reynolds number is defined in 2D as follows:

$$\mathrm{Re} = \frac{\rho d \sqrt{(u - u_d)^2 + (v - v_d)^2}}{\mu}. \tag{102}$$

As to the solution strategy, the operator splitting is used for handling the interaction terms. Equations (91)

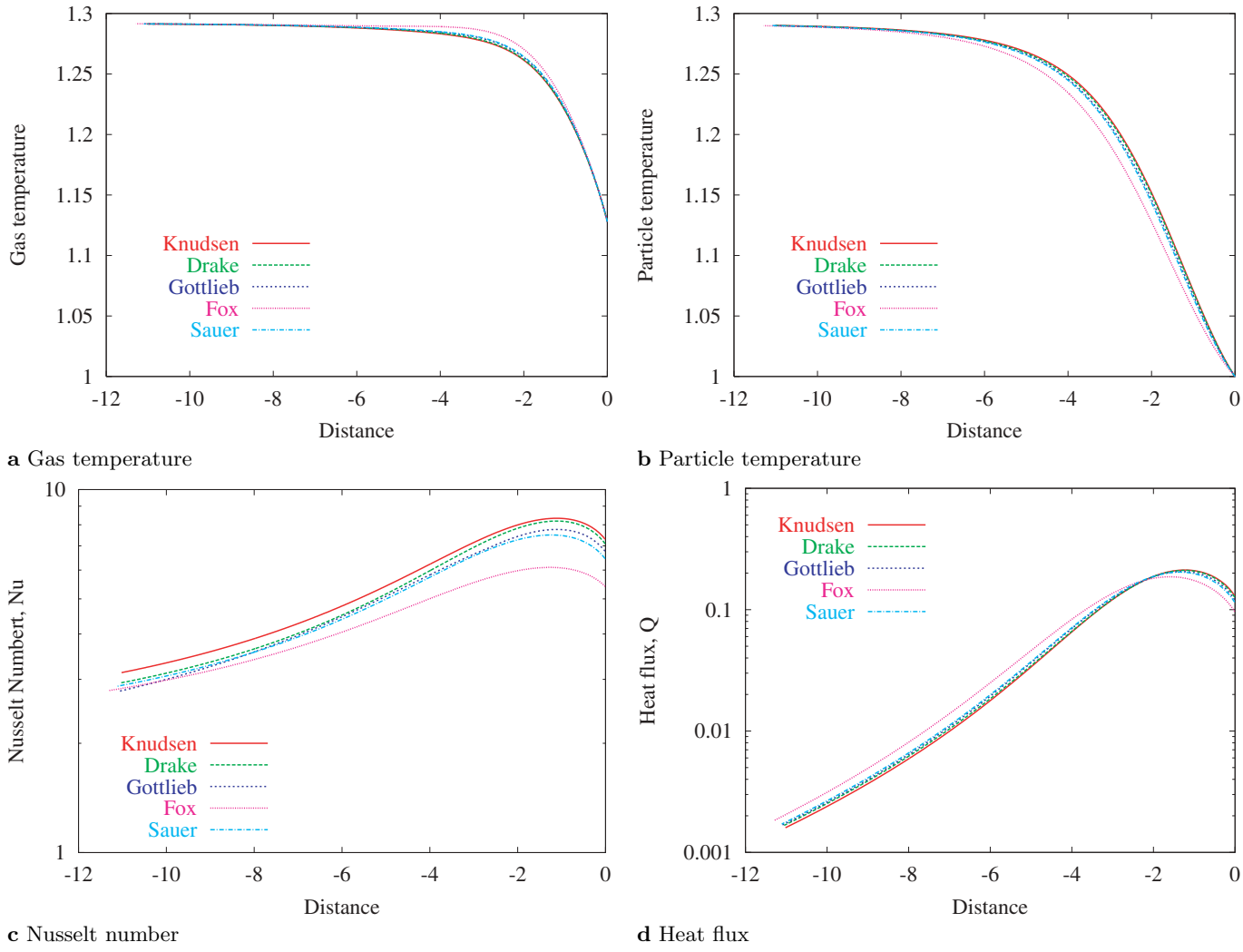

a Gas temperature **b** Particle temperature

c Nusselt number **d** Heat flux

Fig. 19a–d. Effect of different Nusselt number models; $M_{s,f} = 1.2$

and (92) are numerically integrated in two steps as described in Sect. 2.2 for 1D flows:

$$\frac{\partial \boldsymbol{U}_g}{\partial t} + \frac{\partial \boldsymbol{F}_g}{\partial x} + \frac{\partial \boldsymbol{G}_g}{\partial y} = O \ , \tag{103}$$

$$\frac{\partial \boldsymbol{U}_d}{\partial t} + \frac{\partial \boldsymbol{F}_d}{\partial x} + \frac{\partial \boldsymbol{G}_d}{\partial y} = O \ , \tag{104}$$

$$\frac{\mathrm{d}\boldsymbol{U}_g}{\mathrm{d}t} = -\boldsymbol{I} \ , \tag{105}$$

$$\frac{\mathrm{d}\boldsymbol{U}_d}{\mathrm{d}t} = \boldsymbol{I} \ . \tag{106}$$

The homogeneous part of the governing equations, i.e. Eqs. (103) and (104), are solved first and then the solution is further modified by solving (105) and (106), thus taking into account the effect of the interaction between the gas and solid particle phases. When solving (103) and (104), we had an option to use the Strang (1968) operator splitting in multi-dimensional space. In this study, however, the numerical fluxes in both spatial dimensions are considered at once.

For the evaluation of numerical fluxes of the particle phase, Method 1 described in Sect. 2.2.2 is used. The flow parameters are interpolated between neighboring cells as follows:

$$\mathbf{q}(s,0) = \frac{\Delta \mathbf{q}}{\Delta s}\, s + \mathbf{q}^{\circ}, \tag{107}$$

where $\mathbf{q}^{\circ}$ is the initial value at the cell interface:

$$\mathbf{q}^{\circ} = \frac{\mathrm{d}r \cdot \mathbf{q}_l + \mathrm{d}l \cdot \mathbf{q}_r}{\Delta s}, \quad \Delta s = \mathrm{d}l + \mathrm{d}r \ . \tag{108}$$

The interpolated values of flow parameters at the cell interfaces are obtained from the following equations:

$$u_d = \frac{1}{1 + \frac{\Delta u_d}{\Delta s} \cdot t}\, {u_d}^{\circ}, \tag{109}$$

$$v_d = \frac{1}{1 + \frac{\Delta u_d}{\Delta s} \cdot t} \left[\left\{ \frac{\Delta u_d}{\Delta s} \cdot {v_d}^{\circ} - \frac{\Delta v_d}{\Delta s} \cdot {u_d}^{\circ} \right\} t + {v_d}^{\circ} \right], \tag{110}$$

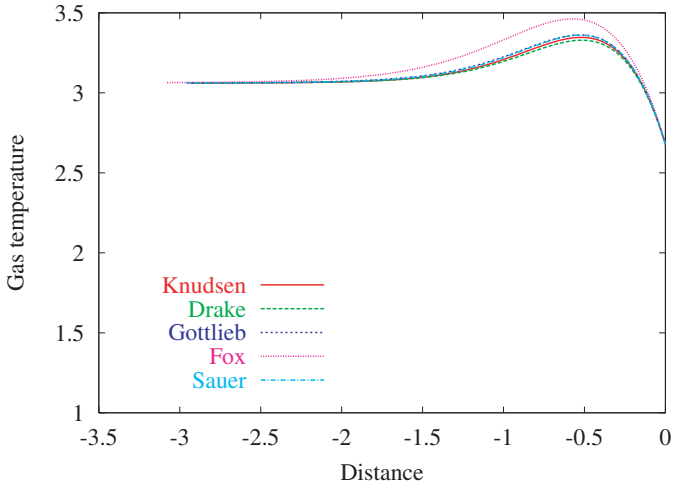

a Gas temperature

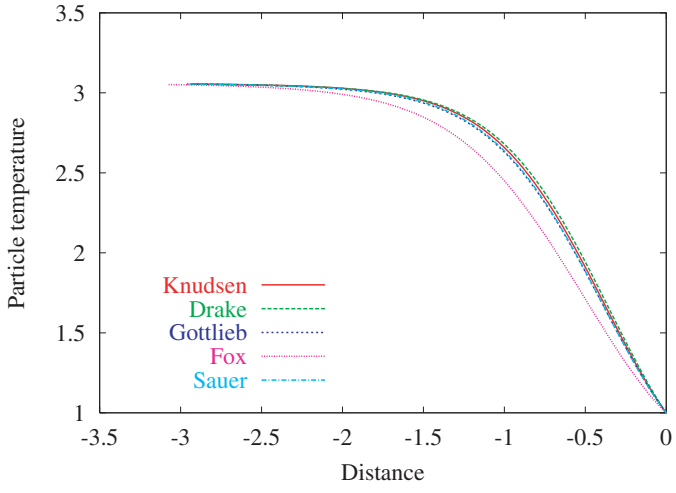

b Particle temperature

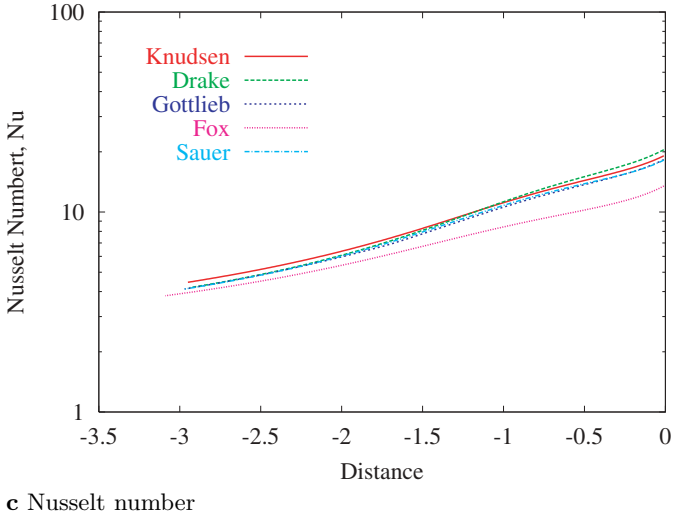

c Nusselt number

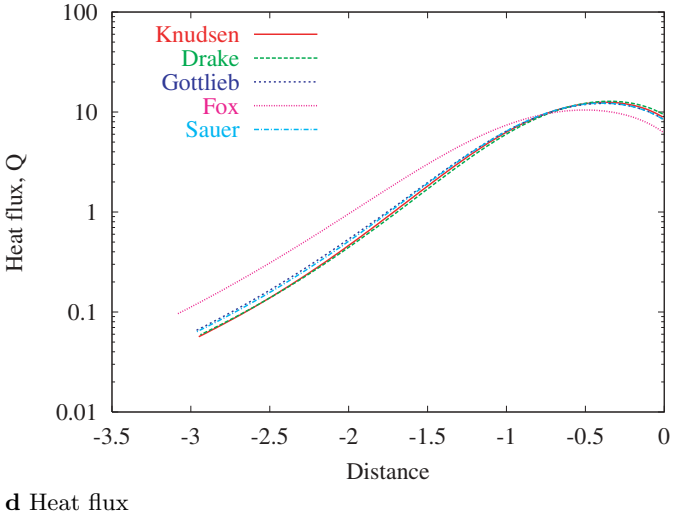

d Heat flux

Fig. 20a–d. Effect of different Nusselt number models; $M_{s,f} = 3.0$

$$\Theta = \frac{1}{1 + \frac{\Delta u_d}{\Delta s} \cdot t} \left[\left\{ \frac{\Delta u_d}{\Delta s} \cdot \Theta^\circ - \frac{\Delta \Theta}{\Delta s} \cdot {u_d}^\circ \right\} t + \Theta^\circ \right], \tag{111}$$

$$\sigma = \frac{1}{\left(1 + \frac{\Delta u_d}{\Delta s} \cdot t\right)^2} \left[\left\{ \frac{\Delta u_d}{\Delta s} \cdot \sigma^\circ - \frac{\Delta \sigma}{\Delta s} \cdot {u_d}^\circ \right\} t + \sigma^\circ \right]. \tag{112}$$

The numerical fluxes at cell interfaces are calculated with the above values at $t = \Delta t/2$.

3.2 Results and discussions

3.2.1 Initial conditions

Figure 21 shows the schematic of the initial conditions corresponding to the plane shock wave reflection from a wedge in a dusty gas. The incident shock wave profile is considered to be fully developed prior to its collision with the wedge. The initial profile is calculated separately by integrating the quasi-steady equations.

The initial and boundary conditions are set as follows:

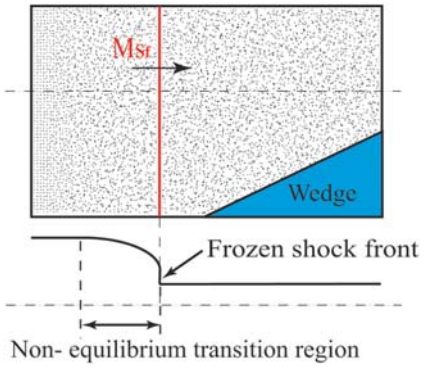

Fig. 21. Schematic of initial conditions

- Ahead of the incident shock wave:
  - Particles are uniformly distributed;
  - Pressure 101.3 kPa;
  - Temperature 300 K;
- Behind the incident shock wave:

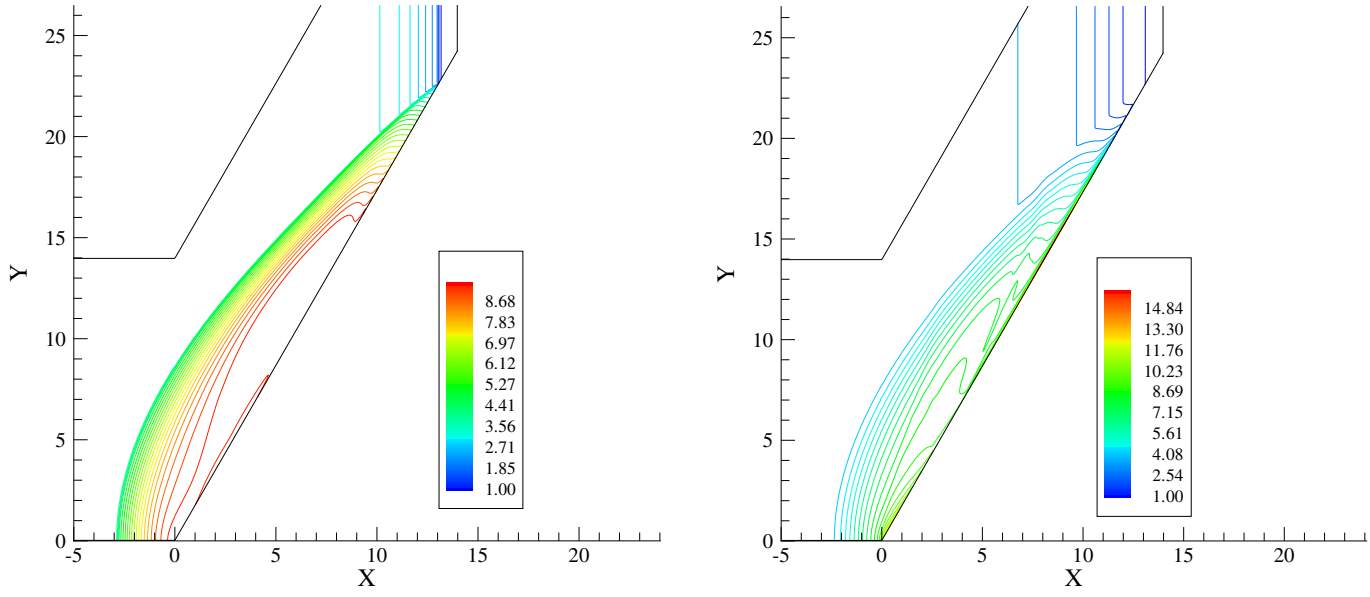

a Gas density **b** Mass concentration of solid particles

Fig. 22a,b. Oblique reflection in dusty gas; $M_{s,f} = 1.5$, $\theta_w = 60^\circ$

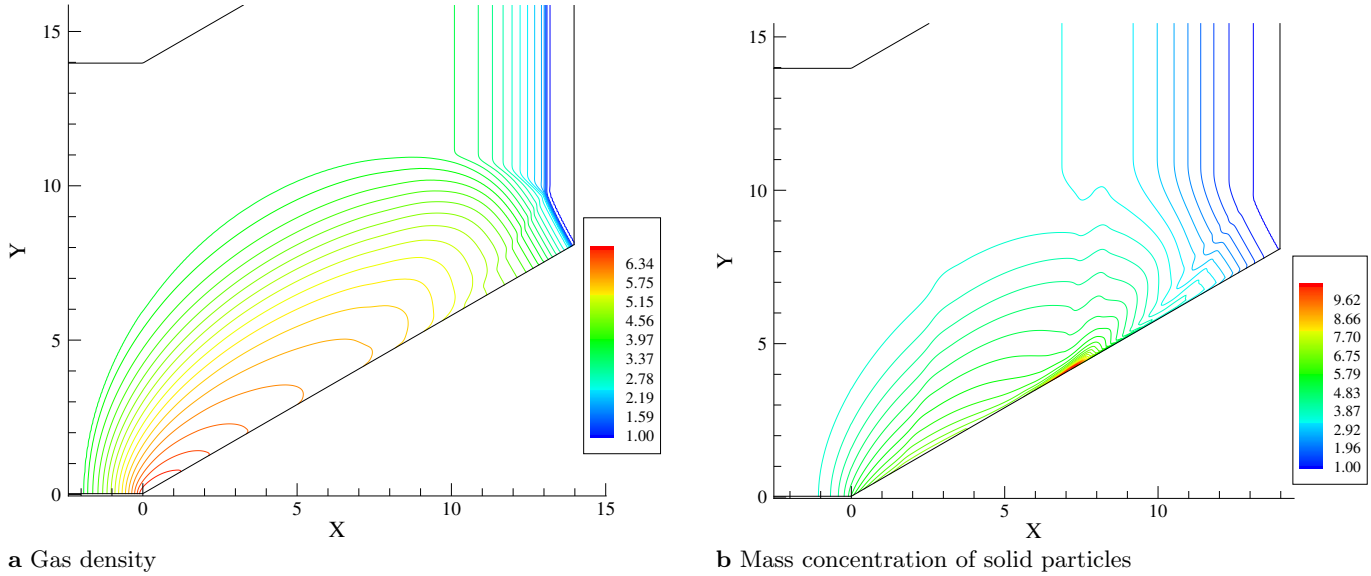

a Gas density **b** Mass concentration of solid particles

Fig. 23a,b. Oblique reflection in dusty gas; $M_{s,f} = 1.5$, $\theta = 30^\circ$

  - The conditions are calculated with the quasi-steady analysis;
- Gas phase:
  - Air ($\gamma = 1.4$);
- Solid particles:
  - Mass ratio of the particles and gas $\alpha = \sigma/\rho = 1.0$;
  - Specific heat ratio of the particles and gas $\beta = C_m/C_v = 1.0$;
  - Diameter of solid particles $d = 10$ μm;
- Boundary conditions:
  - Gas phase: Mirror reflection;
  - Solid particle phase: Sticky wall.

3.2.2 Typical RR and SMR results

Figure 22 shows the gas density and particle concentration distributions for the incident frozen Mach number $M_{s,f} = 1.5$ and the wedge angle $\theta_w = 60^\circ$. The shock wave reflection is of regular type under these conditions. The gas density distribution is quite different from that for a pure gas due to existence of the non-equilibrium area behind the incident and reflected shock waves.

The particle concentration is high near the solid wedge. The gas flow becomes parallel to the solid wall behind the reflected shock wave. The solid particles have much larger

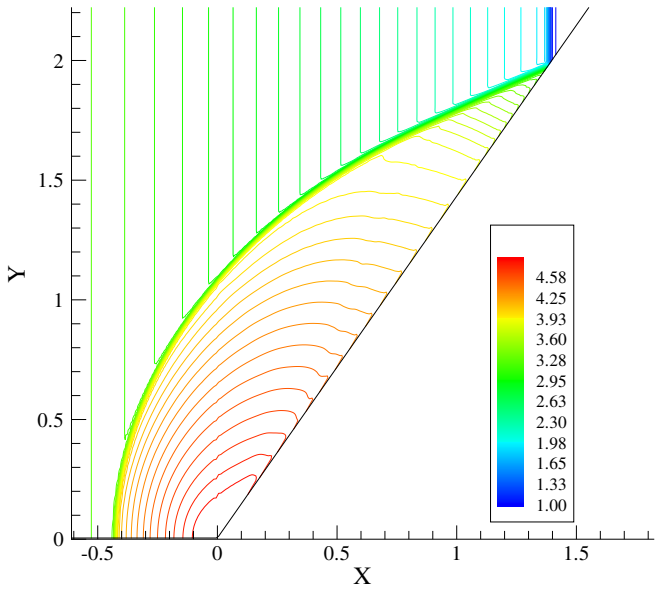

a $\tau = 0.8$

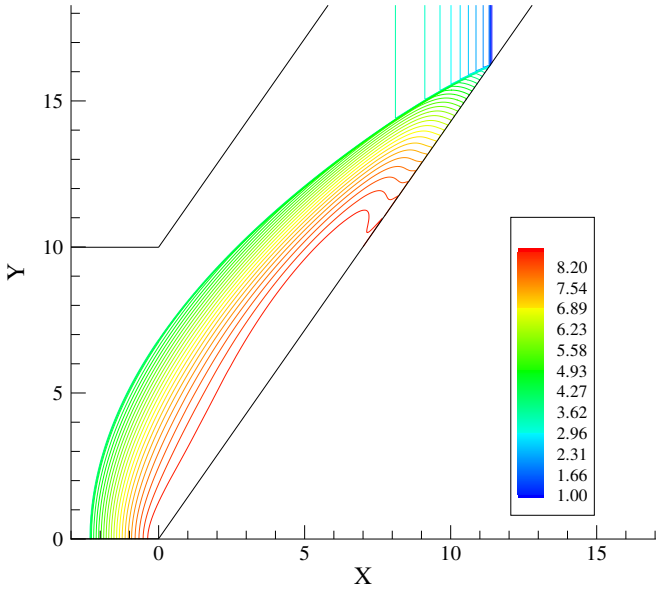

b $\tau = 6.4$

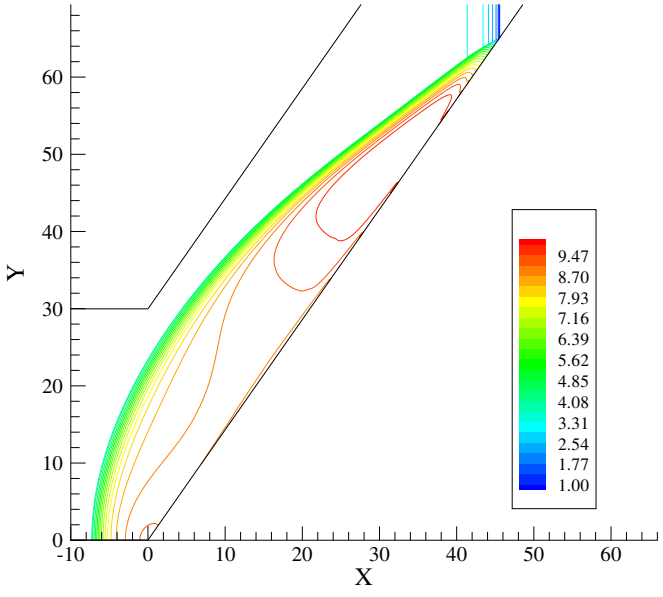

c $\tau = 25.6$

Fig. 24a–c. Transient distributions of gas density; $M_{s,f} = 1.5$, $\theta_w = 55^\circ$

inertia and cannot immediately turn and follow along the wedge surface. They keep approaching the solid wall behind the reflected shock wave. As a result, the mass concentration of solid particles becomes higher near the wall.

Figure 23 shows the gas density and particle concentration distributions for the wedge angle $\theta = 30^\circ$ and the same incident shock Mach number. SMR now appears, with a Mach stem and a slip line in addition to the reflected shock wave. A high-particle-concentration region is seen on the wedge surface.

The directions of dust particle velocities on both sides of the slip line are not parallel due to differences in the way how the particles are accelerated: some are accelerated through the Mach stem, while others – through the incident and reflected shock waves. Therefore, the slip line actually spreads with distance from the triple point. It is, in fact, a slip region, in which the dust concentration is very low.

3.2.3 Non-selfsimilarity

In many cases, oblique shock wave reflections in a pure gas may be considered as self-similar. It is shown both experimentally and numerically (Henderson et al. 2001) that the reflections, even for pure gas cases, are not exactly self-similar due to viscosity and heat transfer on the wedge surface. In a dusty gas, the oblique shock reflection is not self-similar due to the non-equilibrium region behind the shock wave front, even if the effects of viscosity and heat transfer on the reflecting surface are not considered.

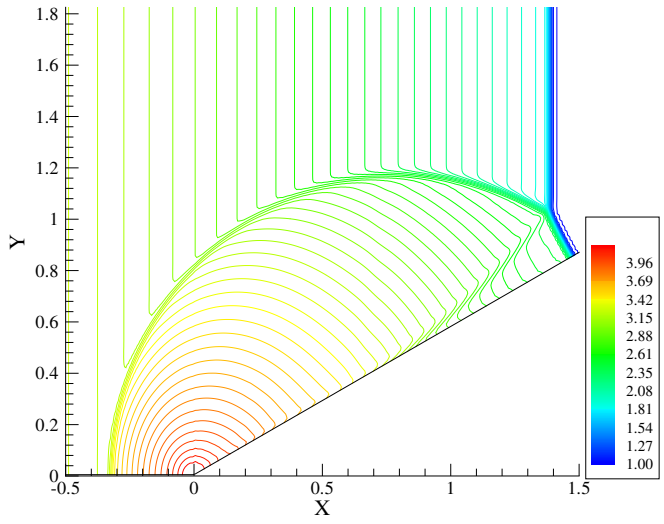

a $\tau = 0.8$

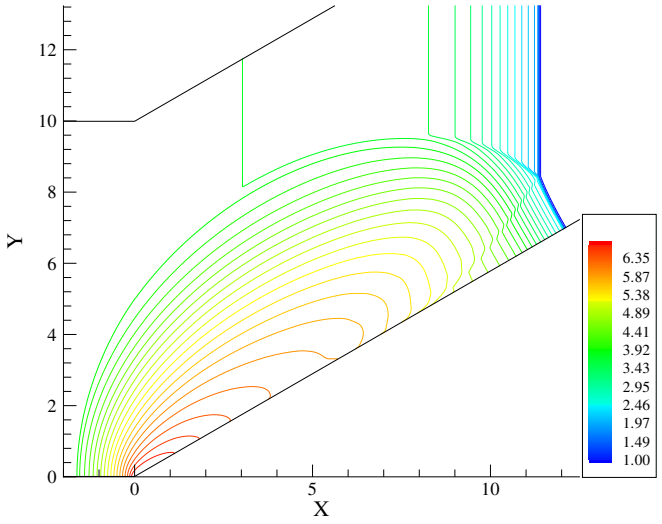

b $\tau = 6.4$

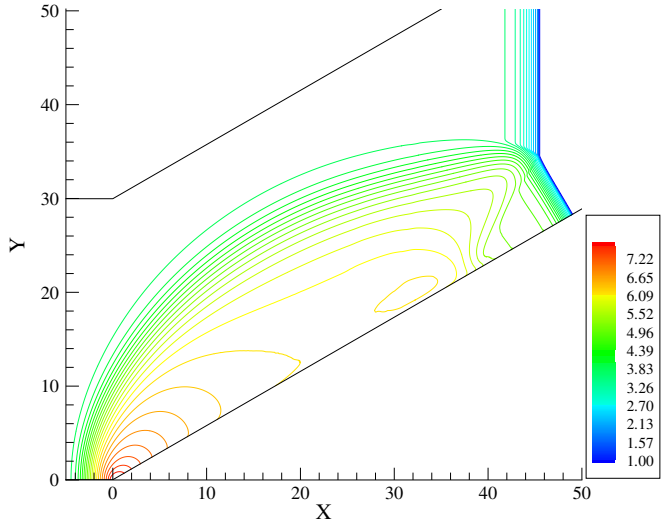

c $\tau = 25.6$

Fig. 25a–c. Transient distributions of gas density; $M_{s,f} = 1.5$, $\theta_w = 30°$

Figures 24 and 25 show RR and SMR at three different time moments. It is clear that the patterns are not self-similar. In 1D case, when a shock wave propagates for a long distance in a dusty gas and once the non-equilibrium post-shock region is established, the shock wave velocity and the extent of the non-equilibrium zone become constant. Therefore, on a large scale, when the width of the non-equilibrium region becomes negligible as compared to the distance travelled by the incident shock, the reflection pattern may be considered as self-similar. However, as seen in the figures, it takes a long time for this situation to be established. For example, assuming the particle material to be crown glass (density 2500 kg/m^3), the non-dimensional time value $\tau = 25.6$ (Fig. 24c) corresponds to 2.5 ms, and the shock propagates 1.4 m during this time interval. Therefore, in most laboratory experiments with dust-gas mixtures the non-equilibrium effects would be significant.

3.2.4 RR-SMR transition

One more consequence of the finite width of the post-shock non-equilibrium region is that the reflection type changes in the course of shock wave propagation. Figure 26 shows the transition from RR to SMR. It takes some time for the Mach stem to be clearly seen. No Mach stem is visible in Fig. 26a, while in Fig. 26d a Mach stem is definitely formed. In pure gas cases, the type of oblique shock reflection is determined by two parameters: the incident shock Mach number $M_{s,f}$ and the wedge angle θ_w. In dust-gas mixtures, the reflection type depends, in addition to $M_{s,f}$ and θ_w, on the distance L_{is} travelled by the incident shock wave along the wedge or its corresponding time t_{is}.

The transition curves in the parametric space of the wedge angle θ_w and the travelled distance L_{is}, for a fixed value of $M_{s,f} = 1.05$, are mapped in Fig. 27. In the figure, the propagation distance is normalized by the characteristic length l defined by Eq. (51) in Sect. 2.2.3, i.e. $l_{is} = L_{is}/l$. The conditions above the curve correspond to RR while SMR is achieved in the area below the curve.

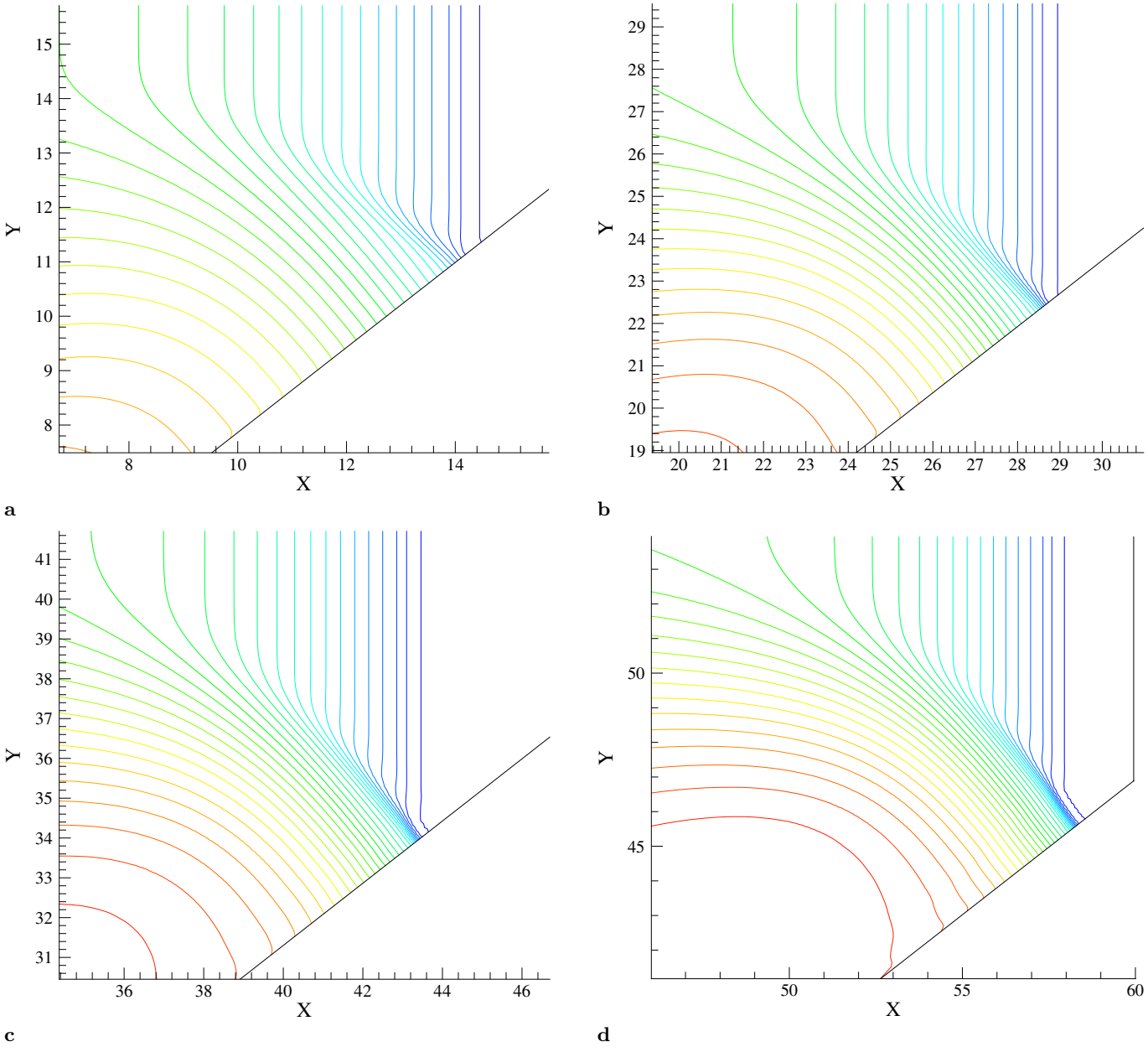

Fig. 26a–d. Transition from regular to Mach reflection; $M_{s,f} = 1.05$, $\theta_w = 38°$

The transition point moves away from the leading edge as the wedge angle increases.

The transition curves in the parametric space of the wedge angle θ_w and the frozen shock Mach number $M_{s,f}$, for a fixed value of $l_{is} = 4.0$, are mapped in Fig. 28. In the figure, the transition curves obtained with the present numerical code for the gas without dust and calculated from the sonic criterion are also shown. The numerical curve of pure gas agrees well with the theoretical curve. The dusty-gas transition curve gives larger wedge angles and the tendency is more pronounced for low Mach numbers.

The sound speed of a dusty gas is slower compared with the same gas without solid particles (see Eq. (56) in Sect. 2.3). Therefore, the signal from the leading edge is delayed and even if SMR occurs in the pure gas, in the presence of dust the pattern may remain to be RR. For higher Mach numbers, however, the temperature behind the shock wave is higher as compared with the pure gas case. Higher temperature increases the sound speed, compensating its decrease due to the presence of dust. Therefore, the deviation of the dusty gas curve from that for the pure gas becomes smaller for higher Mach numbers.

4 Summary

One-dimensional numerical codes for simulating shock wave propagations in dust-gas mixtures were developed. Two

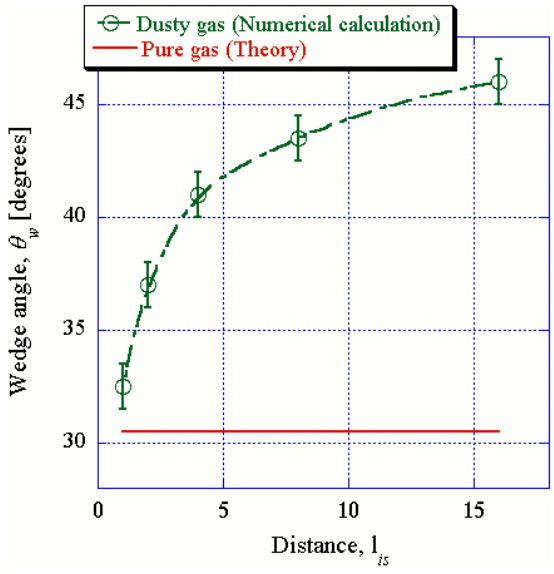

Fig. 27. RR-SMR transition map for $M_{s,f} = 1.05$

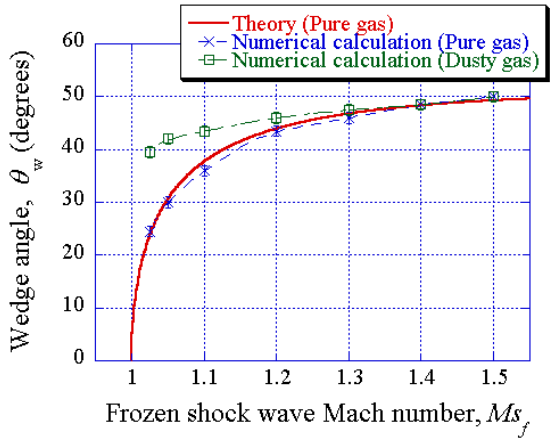

Fig. 28. RR-SMR transition map for $l_{is} = 4$

schemes for evaluating numerical fluxes of the particle phase were compared. It is found that the scheme with the linear interpolation of parameters between adjacent numerical cells is more stable than the other one based on the Riemann problem solution for the particle phase. The scheme with the Riemann problem, however, is useful for studying different boundary conditions of the particle phase at a solid surface since it allows multiple values in numerical cells.

Several models for the drag coefficient between the particle and gas phases were investigated. Within the considered Reynolds number range, all models tested provide similar results, except the models of Stokes and Oseen. These two models were completely out of the range of applicability, and the results were expected.

The effect of different models for the Nusselt number on the shock wave profiles was investigated. It is found that differences in the numerical results were not so significant despite the fact that the complexity of the models differs widely. Taking into account the fact that those models are not fully established, especially for a cloud of dust particles, a reasonable choice should be made, considering computational efficiency and the purpose of the simulations in mind.

The numerical code was extended to two-dimensional problems and applied to oblique shock wave reflections from a solid wedge. The inherent non-selfsimilarity of the phenomena was clearly shown. The transitions from regular to Mach reflection in the course of the incident shock wave propagation along the wedge were also demonstrated, and the respective transition curves were obtained for some values of parameters.

References

Ben-Dor G, Igra O, Wang L (2001) Shock waves reflections in dust-gas suspensions. Trans. ASME J. Fluid Engr. 123:145–153

Carrier GF (1958) Shock waves in a dusty gas. J. Fluid. Mech. 4:376

Chapman S, Cowling TG (1961) The mathematical theory of non-uniform gases. Cambridge University Press

Clift R, Grace JR, Weber ME (1978) Bubbles, drops and particles. Academic, New York

Devals C, Jourdan G, Estivalezes J-L, Meshkov EE, Houas L (2003) Shock tube spherical particle accelerating study for drag coefficient determination. Shock Waves 12:325–331

Drake RM (1961) Discussion on G. C. Vliet and G. Leppert forced convection heat transfer from an isothermal sphere to water. ASME, J. Heat Transfer 83(2):170–179

Falcovitz J, Igra O (2000) Shock wave structure in dusty gas suspension. In: Takayama K, Sun M (Eds) Proc. of the 14th International Mach Reflection Symposium, Yonezawa Japan, 45–58

Fox TW, Rackett CW, Nicholls JA (1978) Shock wave ignition of magnesium powders. In: Ahlborn B, Hertzberg A and Russell D (Eds) Proc. 11th Int. Symp. Shock Tubes and Waves, Seattle: University of Washington Press, 262–268

Fuchs NA (1964) The mechanics of aerosols. Macmillan Company, New York

Gilbert M, Davis L, Altman D (1955) Velocity lag of particles in linearly accelerated combustion gases. Jet Propulsion 25:26–30

Gottlieb JJ, Coskunses CE (1985) Effects of particle volume on the structure of a partially dispersed shock wave in a dusty gas. UTIAS Report Nr. 295

Henderson CB (1976) Drag coefficient of spheres in continuum and rarefied flows. AIAA J. 14(6):707–708

Henderson LF, Takayama K, Crutchfield WY, Itabashi S (2001) The persistence of regular reflection during strong shock diffraction over rigid ramps. J. Fluid Mech. 431:273–296

Igra O, Ben-Dor G (1988) Dusty shock waves. ASME, J. Appl. Mech. Rev. 41(11):379–437

Igra O, Takayama K (1991) Shock tube study of the drag coefficient of a sphere in a nonstationary flow. In: Takayama K (Ed) Proc. of the 18th International Symposium on Shock Waves, Sendai, Japan, Vol.1, 491–497

Igra O, Elperin I, Ben-Dor G (1999) Dusty gas flow in a converging-diversing nozzle. Trans. ASME J. Fluid Engr. 121:908–913

Kim SW, Chang KS (1991) Reflection of shock wave from a compression corner in a particle-laden gas resion. Shock Waves 1:65–73

Knudsen JG, Katz DL (1958) Fluid mechanics and heat transfer. McGraw-Hill, New York

Kriebel AR (1964) Analysis of normal shock waves in particle laden gas. Trans. ASME J. Bas. Engr. pp 655–665

Miura H, Glass II (1982) On a dusty-gas shock tube. Proc. R. Soc. Lond. A 382:373–388

Miura H, Saito T, Glass II (1986) Shock-wave reflection from a rigid wall in a dusty gas. Proc. R. Soc. Lond. A 404:55–67

Nettleton MA (1977) Shock-wave chemistry in dusty gases and fogs: a review. Combustion and Flame 28:3–16

Otterman B, Levine AS (1974) Analysis of gas-solid particle flows in shock tubes. AIAA J. 12(5):579–580

Rudinger G (1964) Some properties of shock relaxation in gas flows carrying small particles. Phys. Fluids 7(5):658–663

Rudinger G (1965) Some effects of finite particle volume on the dynamics of gas-particle mixtures. AIAA J. 3(7):1217–1222

Rudinger G (1970) Effective drag coefficient for gas-particle flow in shock tubes. Trans. ASME, J. Bas. Eng. D 92:165–172

Sainsaulieu L (1995) Finite volume approximation of two phase-fluid flows based on an approximate Roe-type Riemann solver. J. Comp. Phys. 121:1–28

Sauer FM (1951) Convective heat transfer from spheres in a free-molecular flow. J. Aerospace Sci. 18:353–354

Saurel R, Daniel E, Loraud JC (1994) Two-phase flows: second-order schemes and boundary conditions. AIAA J. 32(6):1214–1221

Slater SA, Young JB (2001) The calculation of inertial particle transport in dilute gas-particle flows. Int. J. Multiphase Flow 27:61–87

Soo SL (1967) Fluid dynamics of multiphase systems. Blaisdell Publishing Company, Waltham, Massachusetts

Strang G (1968) On the construction and comparison of difference schemes. SIAM J. Numer. Anal. 5(3):506–517

Thevand N, Daniel E, Loraud JC (1999) On high resolution schemes for solving unsteady compressible two-phase dilute viscous flows. Int. J. Numer. Meth. Fluids 31:681–702

Toro EF (1989) A weighted average flux method for hyperbolic conservation laws. Proc. Roy. Soc. London A 423:401–418

Toro EF (1997) Riemann solvers and numerical methods for fluid dynamics. Springer, Heidelberg